

The performance of BM@N spectrometer

BMN collaboration

February 2023

1 Introduction

BM@N (baryonic matter at Nuclotron) is the first experiment operational at the ion-accelerating complex Nuclotron/NICA, studying interactions of relativistic ion beams of heavy ions with fixed targets [1] in the energy range of high densities of baryonic matter [2]. At the Nuclotron energies, the density of nucleons in a fireball created by two colliding heavy nuclei is 3-4 times higher than the nuclear saturation density [3]. In addition, these energies are high enough to study strange mesons and (multi)-strange hyperons produced in nucleus-nucleus collisions close to the kinematic threshold [4, 5]. The primary goal of the experiment is to constrain parameters of the equation of state (EoS) of high-density nuclear matter. Studies of the excitation function of strange particle production below and near to the kinematical threshold make it possible to distinguish hard behaviour of the EoS from the soft one [6].

The Nuclotron will provide the experiment with beams of a variety of particles, from protons to gold ions, with kinetic energy in the range from 1 to 6 GeV/nucleon for light ions with Z/A ratio of ~ 0.5 and up to 4.5 GeV/nucleon for heavy ions with Z/A ratio of ~ 0.4 .

The BM@N detector is a forward spectrometer covering the pseudorapidity range $1.6 \leq \eta \leq 4.4$. Schematic view of the BM@N setup is shown in Fig. 1. The description of the spectrometer subsystems is organised in a “downstream beam” order. The details for all subsystems are given in a corresponding sections below.

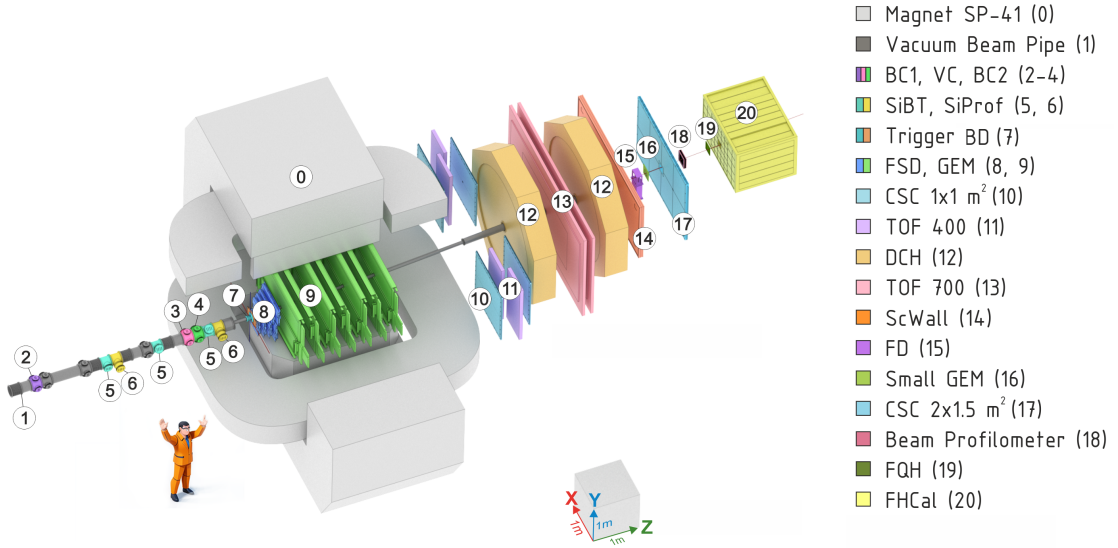


Figure 1: Schematic view of BM@N setup in RUN8.

2 Beamline

2.1 Beam transport

The BM@N experiment is part of the NICA complex (see Fig. 2), located on the extracted beam from the Nuclotron in the target hall.

Electronic string source of the highly-charged ions "KRION-6", provides heavy ions of Au^{31+} (up to 2×10^9 per pulse with a pulse repetition rate of 10 Hz) and delivers them into the HILac.

The main tasks of the booster are as follows:

- accumulation of ions at an injection energy of 2.5×10^9 $^{197}Au^{31+}$ ions;
- effective acceleration of incompletely stripped ions, which is possible due to the ultrahigh vacuum in the beam chamber;
- formation of the required phase volume of the beam using an ECS at an energy of 65 MeV/n;
- acceleration of heavy ions to the energy required for their efficient stripping;
- fast (single-lap) extraction of the accelerated beam for its injection into the Nuclotron.

The Nuclotron SC proton synchrotron has three operation modes:

- Acceleration of heavy ions for storage in the collider.
- Acceleration of polarized protons and deuterons for feeding the collider.
- Acceleration of both polarized and unpolarized protons and deuterons and heavy ions for internal target experiments or slow extraction to fixed target experiments.

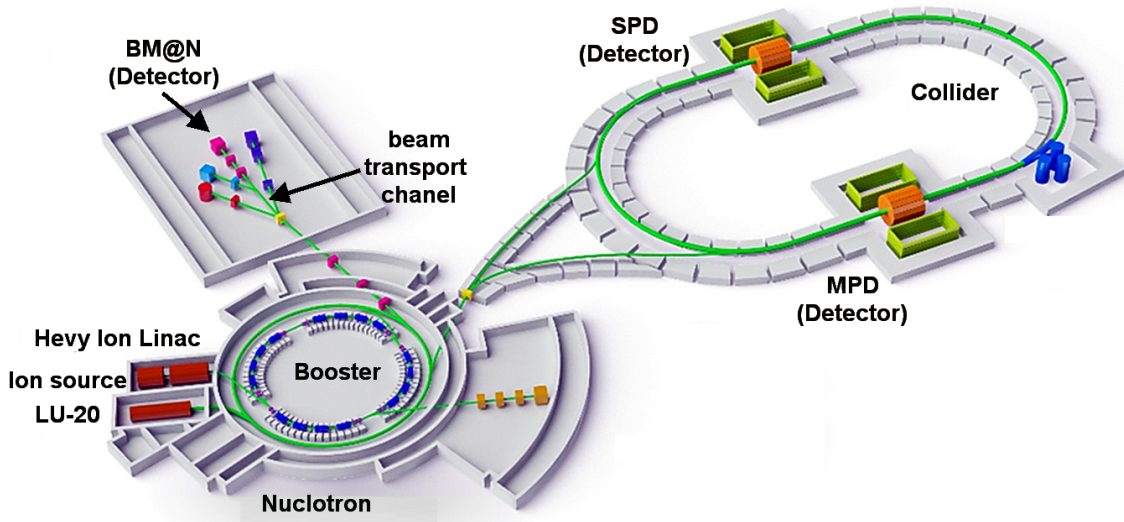


Figure 2: Complex NICA.

The beam extracted from the Nuclotron is transported to the BM@N experimental area over a distance of about 110 m by a set of dipole magnets and quadrupole lenses. At the entrance of the BM@N setup the position and direction of the beam are already close to those required to bring the beam to the target, and only relatively small adjustments are needed in order to provide final steering of the beam. These corrections are performed by a pair of dipole magnets, VKM and SP-57, which allow bending in vertical and horizontal planes and have maximum current 250A and 600A respectively. The centers of these magnets are positioned at approximately 7.7 and 5.7 m from the target (Fig. 3). In addition, a doublet of quadrupole lenses, 1k200 and 2k200, each having the maximum current of 2500A, allows optimal focusing of the beam on the target. The corresponding position of their centers is at about 12.5 and 10.0 m upstream of the target.

The target is located inside the analysing magnet SP-41, therefore, after passing through the target, the beam ions are deflected by the magnetic field of SP-41 (maximum current 2000A, $Bd_l = xxx$ Tm). It should be noted that for experiments with heavy ions it is essential to enclose the beam transport channel in vacuum, including the part that goes through the analysing magnet. This requirement combined with precise placement of the tracking detectors inside the SP-41 does not allow quick reconfiguration of the detectors for different beam momenta, making it necessary to adjust the magnetic field of the analysing magnet depending on the choice of the beam momentum. Studies of the Xe + CsI collisions during the 2022-2023 run were performed at beam energies of 3.0 GeV/n and 3.8 GeV/n, and the current of the SP-41 was set to 1395 and 1720 A respectively.

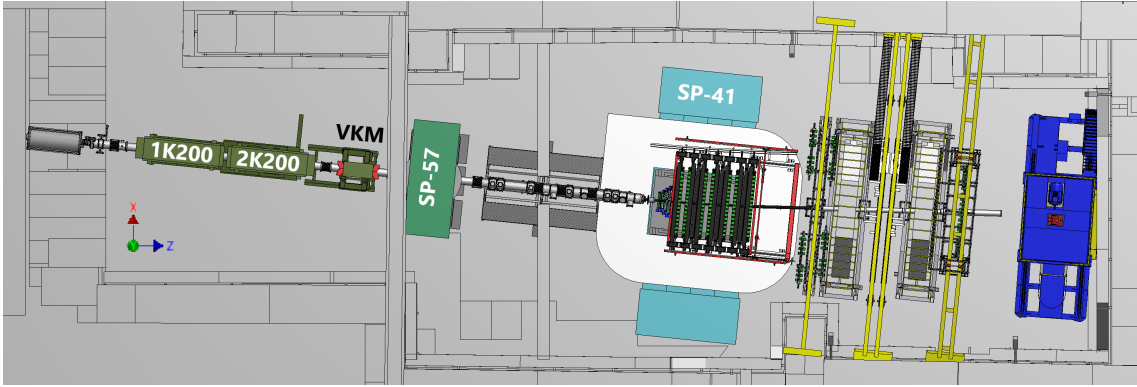


Figure 3: Magnetic elements of the BM@N setup.

59 2.2 Vacuum beam pipe

60 A vacuum beam pipe was integrated into the experimental setup in order to minimize the amount
 61 of scattering material on the way of heavy ion beam. The beam pipe has continuous vacuum, but
 62 in terms of components and material of the tube it can be subdivided into four large parts: the first
 63 section covers the region upstream of the magnet SP-57 and within the magnet itself, the second
 64 section goes up to the target, the third section is placed inside the analyzing magnet SP-41 and the
 65 last section is located after the analyzing magnet. Vacuum in the entire beam pipe at the BM@N
 66 setup is achieved by a single roots pump installed upstream of the 1K200 quadrupole lens. The
 67 pressure maintained during the experiment is at the level of 10^{-4} Torr. With the exception of the
 68 third part, the configuration of vacuum pipe and its components were designed, manufactured and
 69 tested by LLC Vacuum systems and technologies (Belgorod, Russia). ISO-K vacuum standard is
 70 accepted for flange connections, however, significant fraction of the components was custom made
 71 in order to meet limitations posed by aperture of the magnets and geometry of the detectors.

72 The first part of the beam pipe is designed to create vacuum in the area of beam transport
 73 through 1K200 and 2K200 quadrupole lenses and through corrective magnets VKM and SP-57.
 74 This part of the vacuum pipe is made of stainless steel, has length of 11.7 m and outer diameter
 75 200mm. Two slide gates are installed in this section, one in the front of the 1K200 lens and
 76 another after the VKM magnet. The vacuum level is monitored by two vacuum gauges, the data
 77 from which are recorded in the slow control system.

78 The second part of the beam pipe serves to create vacuum in the region between the SP-57
 79 magnet and the target node located inside the SP-41 magnet. This part of the beam pipe is xxx
 80 m long and also has outer diameter 200mm. It includes vacuum boxes containing beam detectors
 81 described in the next section: two 3-way boxes for profilometers, three 3-way boxes for silicon
 82 tracker and three 6-way boxes for trigger counters BC1, BC2 and VC. All boxes located outside
 83 the magnetic field of the analyzing magnet SP-41 are made of stainless steel, while the vacuum
 84 pipe components, which have to be close to the target and therefore placed in the magnet, are
 85 made of aluminum: compensator and three boxes for profilometer, Si beam tracker and BC2.
 86 Bending of the beam ion trajectories by the magnetic field leads to a deflection from a straight line
 87 resulting in a few mm displacement in X direction at the target location. During the assembly of
 88 vacuum elements of the beam pipe, an adjustment is carried out in order to compensate for this
 89 deflection. For that purpose the corresponding grooves for O-rings of the vacuum boxes are made
 90 slightly wider than dictated by the ISO standard and allow slight off-center shifts of the vacuum
 91 pipe components. The target flange assembly is also made of aluminum as well as an ISO240 to
 92 66 mm vacuum adapter for connection with the vacuum tube of the third section.

93 The third part of the beam pipe is 4.5 m long and made of carbon fiber by so-and-so producer.
 94 The entire carbon pipe consists of four straight segments of different lengths connected to each
 95 other by flangeless carbon fiber connections, which provide possibility to align sections at slight
 96 angles with respect to each other as shown in Fig. 4 and 5. The rotation angles were evaluated
 97 by the simulation of the 4.5 AGeV (???) gold ions trajectories in the magnetic field of SP-41 at
 98 current xxx A. The carbon beam pipe is suspended on two supports also made of carbon fiber and
 99 installed on two lower GEM detectors, the one closest to the target and the most downstream. The
 100 supports have adjustment units for precise positioning of the carbon beam pipe on the beam axis
 101 (Fig. 5). The carbon beam pipe was designed to sustain vacuum up to 10^{-4} Torr. In the straight
 102 segments the thickness is about 1 mm, while in flangeless connections it reaches 2 mm.

103 The fourth part of the beam pipe provides vacuum volume along the beam trajectory through

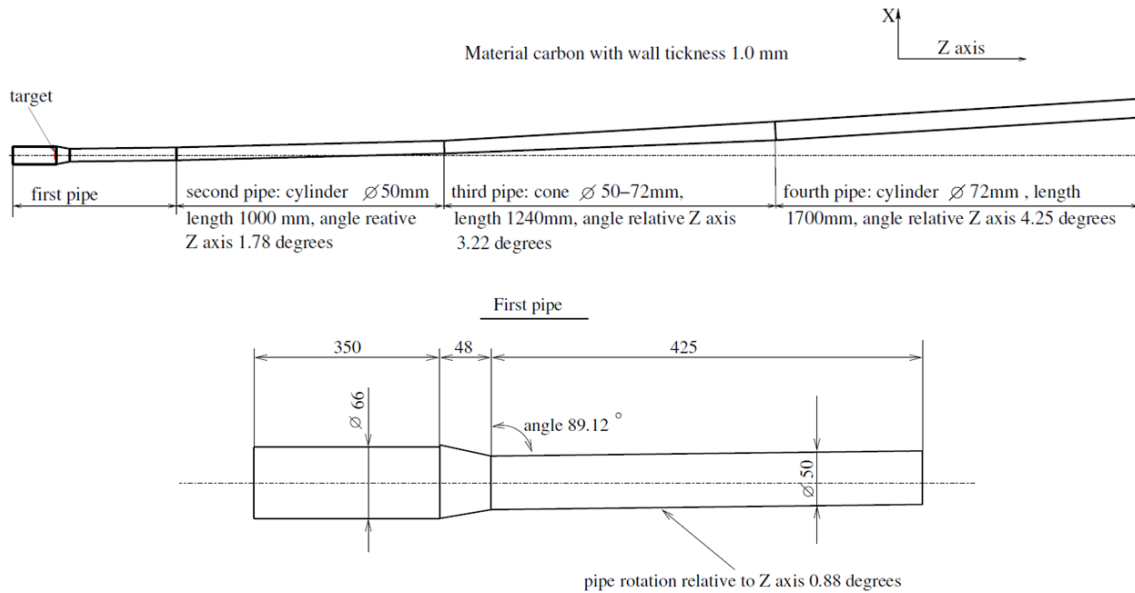


Figure 4: Technical design of the carbon beam pipe.

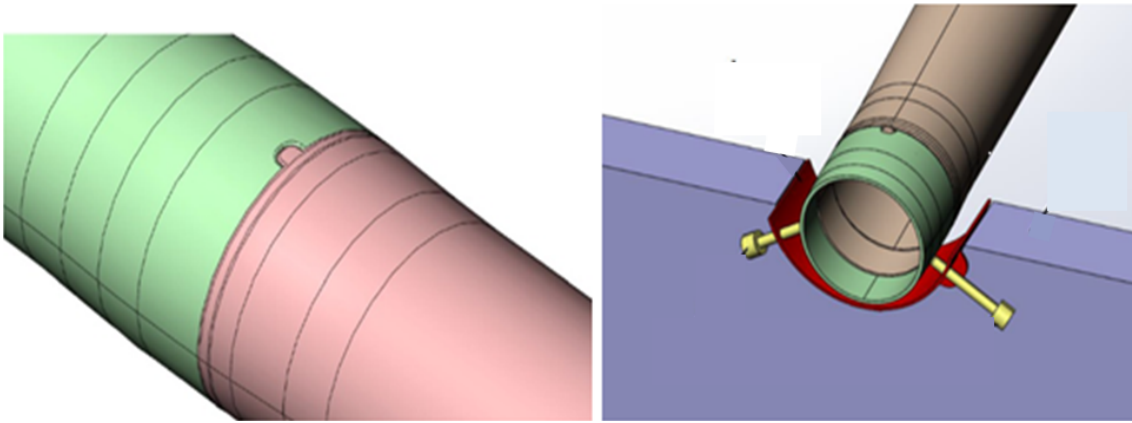


Figure 5: 3D models of the dismountable flangeless connection (left) and the support scheme of the carbon beam pipe in the GEM beam hole (right).

104 the outer tracker system. The pipes and flanges of this section as well as connection to the carbon
 105 beam pipe are made from aluminum (Fig. 6). It has overall length of about 3.2 m (?) and consists
 106 of three straight segments 1.2, 0.96 and 1.0 meter long, made from tube with outer diameter of
 107 125 mm and wall thickness of xx mm. At the end of this section, the overall vacuum line is closed
 108 by a 100 μm thick titanium membrane installed in ... (?) after the adapter for a diameter of 150
 109 mm.

110 2.3 Target station

111 The target station is located at the end of the second beam pipe section. It is designed to provide a
 112 possibility to insert a target in the beam line inside the vacuum volume and to interchange several
 113 targets without breaking the vacuum. The model and photo of the target station are presented
 114 in (Fig. 7). An aluminum flange of 240 mm in diameter serves as a holder of the target assembly
 115 elements and as an adapter between the beam pipe upstream of the target station and the first
 116 section of the carbon beam pipe. On the outer part of this flange, four pneumatic cylinders are
 117 installed providing capability to move in and out of the beam four target frames interchangeably.
 118 The pneumatic cylinders are produced by FESTO and allow remote operation. An optocoupler
 119 sensor is used in order to control the target position via a special electronic module.

120 The part of the target assembly placed inside the vacuum can be divided into three components:
 121 1) Centering frame, which fits into the inner part of the first section of the carbon beam pipe.
 122 2) Four petals, in which the targets themselves are installed. In the normal state, all petals are
 123 leaning against the side surface of the beam pipe.



Figure 6: Carbon beam pipe connected by a flange to aluminum beam pipe in the BM@N setup.

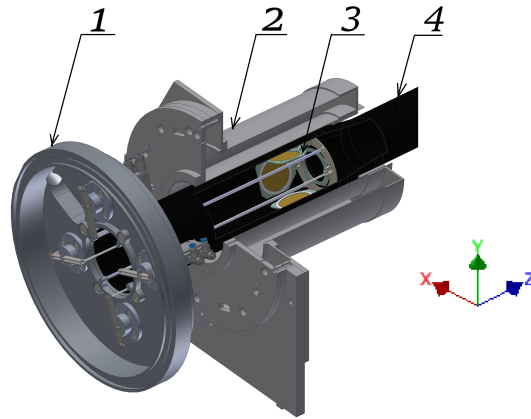


Figure 7: 3D model of target station. 1. Aluminum flange target station. 2. Barrel detector. 3. four targets. 4. Carbon beam pipe.

3) Carbon fiber retaining pins, 300mm long and 3mm in diameter.

In the run with the Xe beam, three disk targets about 3.2 cm in diameter were used: CsI 1.75mm thick, CsI 0.85 mm thick, and Ge 1.02mm thick. One frame of the target assembly was left empty and was used to evaluate the background level caused the particles interactions with the structural elements of the target station.

2.4 Magnetic field of the analysing magnet

The dipole magnet SP-41 with large acceptance is used in the spectrometer as analysing magnet for measurement of momenta of produced particles and beam fragments. In the course of preparation of the magnet for the BM@N experiment, significant upgrade was done in 2012-2013 from SP-41 initial configuration used in the experiments with a streamer chamber. In particular, the hole for a photcamera in the upper pole was filled with steel in order to improve the uniformity of the magnetic field, and the distance between the poles was increased by about 30 cm in order to provide space required by the GEM chambers of the BM@N. The dimensions of the SP-41 pole in the horizontal direction and in the direction along the beam is about 1.4 and 2.5 m, respectively, while the vertical distance between the upper and lower poles after the upgrade is 1.06 m (Fig. 8). In the BM@N setup the magnet is roughly centered on the beam line, in the horizontal plane the beam axis goes through the magnet close to the center of the poles, while vertically the beam axis is shifted closer to the lower pole by about 40 mm. The leading edge of the pole defines the origin of the z axis, and, correspondingly, the target is installed inside the SP-41 magnet at this position along the beam. The target station is described in more detail in the chapter Targets.

Determination of the momentum of the produced particles requires detailed knowledge of the value and orientation of the magnetic field of the analysing magnet. After the upgrade of the SP-41, the measurement of its field was performed by means of planar and 3D Hall probes [7]. In addition, the shape of the field was calculated by the TOSCA code using known configuration of the yoke and coils material. Prior to the run with Xe beam, in Spring 2022, the measurement of the magnetic field was repeated with a goal to obtain the field map for a wider X, Y, Z range and with

150 smaller steps. The measurements with 3D Hall probes covered (-156, +145 cm), (-38, +54 cm),
 151 (-162, +439 cm) and were performed in (126 x 47 x 241) points in X, Y, Z coordinates respectively,
 152 allowing one to construct the field map on a $2.4 \times 2.0 \times 2.5 \text{ cm}^3$ three-dimensional grid (Fig. 8).
 153 During simulation and event reconstruction, the magnetic field components in a particular (x, y, z)
 154 point are calculated by linear interpolation over eight neighboring measured nodes.

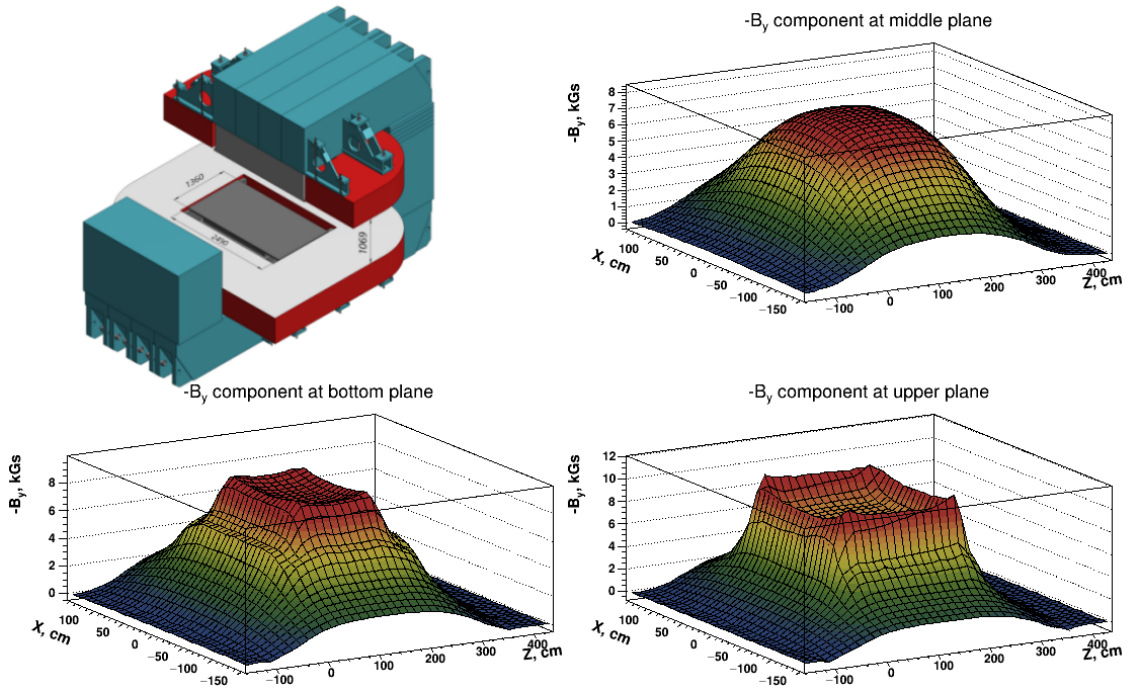


Figure 8: Magnetic field map of the analyzing magnet SP-41.

155 The measurements of the field map was performed for four values of the current: 900, 1300,
 156 1600, and 1900 A.

3 Beam and trigger detectors

Fig. 9 shows a schematic layout of the trigger detectors, placed on the beam line. In the target area the multiplicity detectors are also shown as a part of the trigger system.

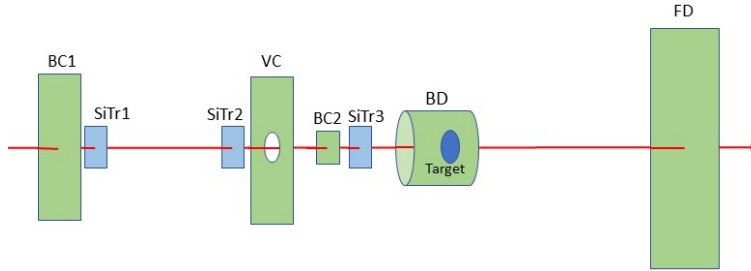


Figure 9: Trigger detectors layout.

Some physical parameters of the beam line detectors are summarized in Table 1.

Aperture of the beam is limited by the 25 mm diameter hole in the scintillation Veto Center (VC), which rejects the beam halo. The hole diameter in VC is chosen to be large enough to accept most of the beam ions, but smaller than the diameter of the target XX mm. Typically, in the 2023 Xe run, 80% of the beam was accepted by the VC. In order to minimize interactions upstream of the target, scintillators and active parts of silicon detectors are located in vacuum, while the photomultiplier tubes of the scintillation counters and the front-end electronics of the silicon detectors are kept in the air with their housings mounted to the flanges of the beam pipe.

Detector	Z position, cm	Active area, mm x mm	Material	Thickness, mm
BC1	-zz	100 x 100	Scint. BC400B	0.25
BC2	-zz	34 x 34	Scint. BC400B	0.15
VC	-zz	113 x 113 (hole 25)	Plastic	4
SiBTr1	-283	61 x 61	Silicon	0.175
SiBTr2	-183	61 x 61	Silicon	0.175
SiBTr3	-84	61 x 61	Silicon	0.175
FD	+784	150 x 150	Scint. BC408	0.5
Small GEM	+793	100 x 100		
FQH	+970	160 x 160	Quartz	4

Table 1: Parameters of beam and fragment detectors.

In all the beam scintillation counters - BC1, BC2 and VC - light from the scintillator is collected by Al-mylar light guides to a pair of photo-multiplier tubes, placed above and below the scintillator. Such orientation of PMT's in BC2 and VC detectors is dictated by the requirement that they should operate in the magnetic field of the analysing magnet, because these counters are located close to the target. Mesh dynode photomultiplier tubes Hamamatsu R2490-07 are used in the detectors BC1 and VC, whereas the BC2 has microchannel plate PMT's Photonis XPM85112/A1 Q400. In addition to beam geometry, the detectors BC1 and BC2 define start time for the time-of-flight system. The requirement to obtain precise time measurement favored the design of BC1 and BC2 with light collection by two PMT's. Both types of photo-multiplier tubes used in these counters have excellent timing characteristics. The signal from each PMT is sent to a fast fan-out module which has time jitter of about 10 ps and preserves high quality of time response. The signal from one output of the fan-out is sent to a TQDC which allows to determine time and amplitude of the pulse. After correction for time walk (slewing), the resolution obtained in 2022 Xe run using the signals from both photo-tubes was found to be 40 ps for BC1 and BC2 individually, and 30 ps for the combined response of the system of two counters. The input in the trigger logic is configured to accept one signal from each of the beam counters, BC1, BC2 and VC. Individual signals from top or bottom PMT's are affected by light collection non-uniformity to a larger degree than a combined signal from two photo-tubes. Therefore, in all counters the signals from top and bottom PMT's are balanced in gain by high-voltage settings, and the signals from the second output of the fan-outs are sent to a passive linear fan-in after which the summed signals are fed to the trigger logic unit. In addition, the summed signals are read-out using TQDC for trigger setting up and monitoring.

190 Upstream the target the beam position is traced by a set of silicon tracker detectors. The
 191 beam tracker system consists of three double-sided silicon strip detectors identical in design. Each
 192 detector has 60 mm by 60 mm active area with orthogonal orientation of p+ and n+ strips on two
 193 sides. These detectors are kept permanently in the beam and provide information about beam
 194 ion trajectory for each event. More detailed description of the beam tracker is given in the next
 195 chapter. In addition to the beam tracker, the beam position and profile can also be measured
 196 by a pair of beam profilometers which are similar in design and parameters to the beam tracker
 197 stations, but have a much courser pitch 1.8 mm in X and Y. The read-out of the profilometers is
 198 organised independently of the main BM@N DAQ in order to facilitate beam tuning at the early
 199 stages of the run. The detectors of the beam profilometers can be moved in and out of the beam
 200 by remotely controlled drivers without breaking the vacuum. During the data accumulation the
 201 detectors of the beam profilometers are positioned outside of the beamline.

202 Trigger detectors sensitive to the multiplicity of particles produced in the interaction include
 203 Barrel detector (BD) and Silicon multiplicity detector (SiMD). These detectors, schematically
 204 shown in Fig. 10, are placed close to the target in order to cover sufficiently large solid angle for
 205 produced particles. The target is situated inside the BD.

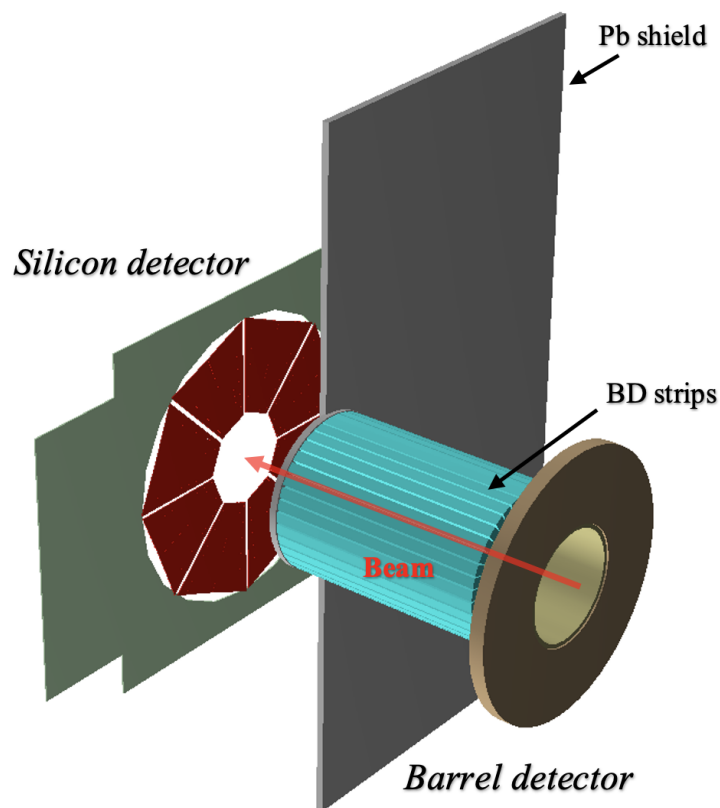


Figure 10: Schematic layout of trigger multiplicity detectors.

206 The Barrel detector is formed by 40 scintillator strips aligned along the beam line and covering
 207 cylindrical surface 90mm in diameter and 150mm long. Each strip of $150 \times 7 \times 7 \text{ mm}^3$ size is
 208 coated with aluminized mylar and viewed from one side by a silicon photo-multiplier of $6 \times 6 \text{ mm}^2$
 209 size (SensL, J-ser.).

210 Downstream the analysing magnet the beam goes through the Fragment Detector (FD), Small
 211 GEM chamber and the Forward quartz hodoscope (FQH). These detectors are placed in the air,
 212 the FD is positioned right after the titanium membrane which closes the vacuum pipe line. The
 213 amplitude of the pulse in the FD reflects the charge of the ion passing through the counter. This
 214 amplitude is used in the trigger system in order to distinguish events with and without interactions
 215 in the target. To minimize the background from the interaction within the FD itself, its radiator
 216 has to be thin, while in the X and Y directions the radiator should be wide enough to cover all
 217 the beam ions going through the target without interaction. The radiator material can be chosen
 218 either from scintillator or quartz in experiments with relatively light (up to Xe) or heavy (Au, Bi)
 219 beams respectively. For most of data accumulation in the Xe 2022 run the scintillator radiator was
 220 used, while the quartz radiator was also evaluated in the short period of the run. The radiator was

221 viewed by a single photo-multiplier tube placed about 50 cm below the beam line. Light collection
222 is done by an air light guide made of aluminized mylar. Pulse height resolution of the FD with the
223 scintillator radiator was found to be 5% for Xe peak.

224 In addition to the FD the charge of spectator fragment can be determined by the 4mm thick
225 quartz hodoscope FHQ, located in front of the beam hole in the FHCa. Information from this
226 hodoscope is used in the offline analysis for event selection and determination of event centrality.
227 FHQ amplitude resolution for Xe ions is about 2%. The detailed description of the hodoscope is
228 given in the section "Forward Spectator Detectors".

229 The Small GEM detector is positioned between the FD and FHQ and used to monitor the
230 position, shape and spot size of the beam downstream the analysing magnet. The detector has
231 three GEM foils. Its active area covers 10 cm \times 10 cm in X and Y, with 256 strips in each coordinate
232 oriented perpendicular to each other.

233 **4 Silicon Beam Tracker**

234 As already mentioned in the previous section, the main task of the Silicon Beam Tracker (SiBT) is
 235 to measure the beam ion trajectory in each event and determine primary vertex coordinates and
 236 impact angle of the beam projectile. The tracker consists of three stations each of which utilizes a
 237 double-sided silicon strip detector (DSSD) with dimensions $(63 \times 63 \times 0.175)mm^3$. DSSD planes
 238 are cut from high-resistivity mono-crystalline silicon obtained by the Float Zone method. The
 239 thickness $175 \mu m$ was chosen as the minimum possible, taking into account the limitations of the
 240 planar technology applied to 4" (100 mm) wafers. The minimum thickness of the planes allows
 241 not only to reduce the amount of material in the beam, but also to decrease the volume of space
 242 charge region of the detector and thus to lower the noise caused by the radiation defects per strip,
 243 which is very important considering that the detectors are exposed to heavy ion beams of high
 244 intensity.

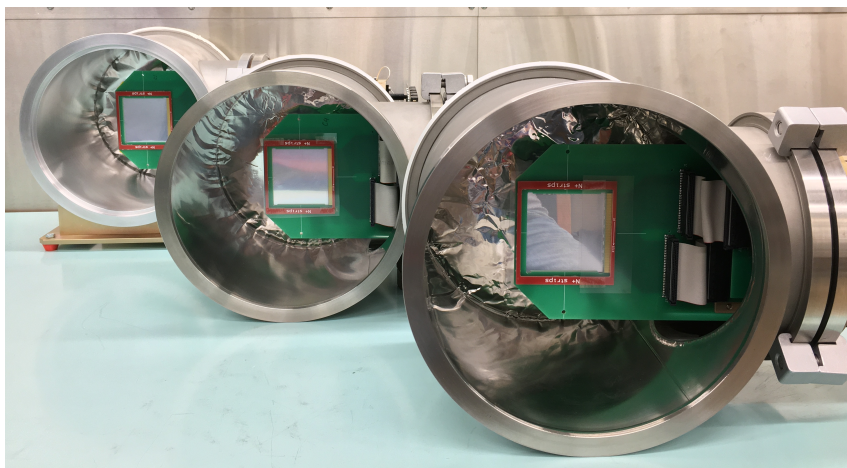


Figure 11: Three stations SiBT1, SiBT2, SiBT3 with detectors and FEE electronics, view along the beam (n^+ side of the strips).

245 The active area in each of the detectors is $(61 \times 61)mm^2$, and the pitch between strips is
 246 $470 \mu m$ on both, p^+ and n^+ , sides resulting in total 2×128 readout channels. The strips on
 247 two sides are oriented orthogonally with respect to each other. The silicon plate in the SiBT1
 248 detector is positioned inside the beam pipe such that the strips are aligned along the X and Y
 249 axes, whereas the plates of the SiBT2 and SiBT3 detectors are rotated azimuthally by 30 and 60
 250 degrees respectively.

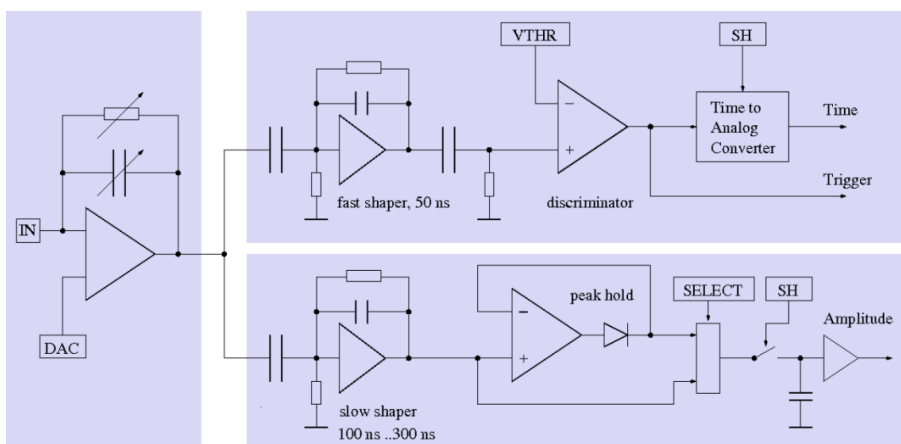


Figure 12: Block diagram of the VATA64HDR16.2 chip for the detector electronics of the beam tracker.

251 Figure 11 shows three vacuum stations with DSSD coordinate planes installed inside. The
 252 positions of the coordinate system of each DSSD plane relative to the geometrical axis of the beam
 253 pipe were measured using a NORGAV NVM II-5040D video meter with an accuracy of $\pm 5 \mu m$.
 254 Structurally, the detectors are assembled on printed circuit boards with gold contact pads, which

255 are connected by ultrasonic bonding with Al-plated strips on the DSSD surface. The signals from
 256 the detector strips in four groups of 64 channels are sent via flat cables to vacuum connectors (4
 257 connectors) fixed in the vacuum flange. The front-end-electronics (FEE) for 128 p^+ and 128 n^+
 258 strips is mounted on the flange outside the vacuum volume. The detector electronics in this case
 259 is practically outside of high radiation zone and is available for testing and, if needed, replacement
 260 without breaking the vacuum in the beam pipe.

261 Figure 12 shows a block diagram of the integrated circuit VATA64HDR16.2 (IDEAS, Norway),
 262 chosen for the FEE because of its large dynamic range ($-20pC \div +50pC$) suitable for operation
 263 with beams of highly ionizing heavy ions. For example, charge in the input signal caused by 3-4
 264 GeV/nucleon Xe ion going through a 175 μm layer of silicon is 11 pC.

265 The ASIC VATA64HDR16.2 accepts up to 64 input channels, therefore, four of the chips are
 266 used in each of the SiBT stations. After passing through pulse shapers, at the time defined by
 267 "external trigger - SH", the values of signal amplitudes from 64 strips are stored on the mem-
 268 ory capacitors. After that, in sequential reading mode using an analog multiplexer, the 64 sig-
 269 nals are transmitted for digitization into a single ADC channel. The main parameters of the
 270 VATA64HDR16.2 chip are given in Table 2.

Number of channels	64
Input charge dynamic range	$-20pC \div +50pC$
Read-out signal generation time	50ns, 100ns, 150ns, 300ns, programmable
Trigger	1 trigger output (Trigger-OR)
Trigger signal generation time	50ns
Equivalent Noise Charge (ENC)	1fC without load
Adjustable trigger threshold	External + 4-bit threshold trim-DAC/ch.
Gain	2-gain settings, programmable
Output	Single analog multiplexed output of 64 pulse height samples
Power consumption per ASIC	960mW max. depending on settings
Voltage supply	+2.5V, -2.5V

Table 2: Main parameters of VATA64HDR16.2 chip.

271 Figure 13 illustrates three stations of the beam tracker mounted in the vacuum beam pipe of the
 272 BM@N channel. Histograms shown at the bottom part of the figure represent online monitoring
 273 of 2D distribution of beam ion hits in the tracker. Typical RMS of beam profile in the 2023 Xe
 274 run, measured for trigger selected events, i.e. for ions passing through the 2.5 cm dia. hole of the
 275 Veto Counter, was 0.5 cm and 0.6 cm in X and Y coordinates respectively.

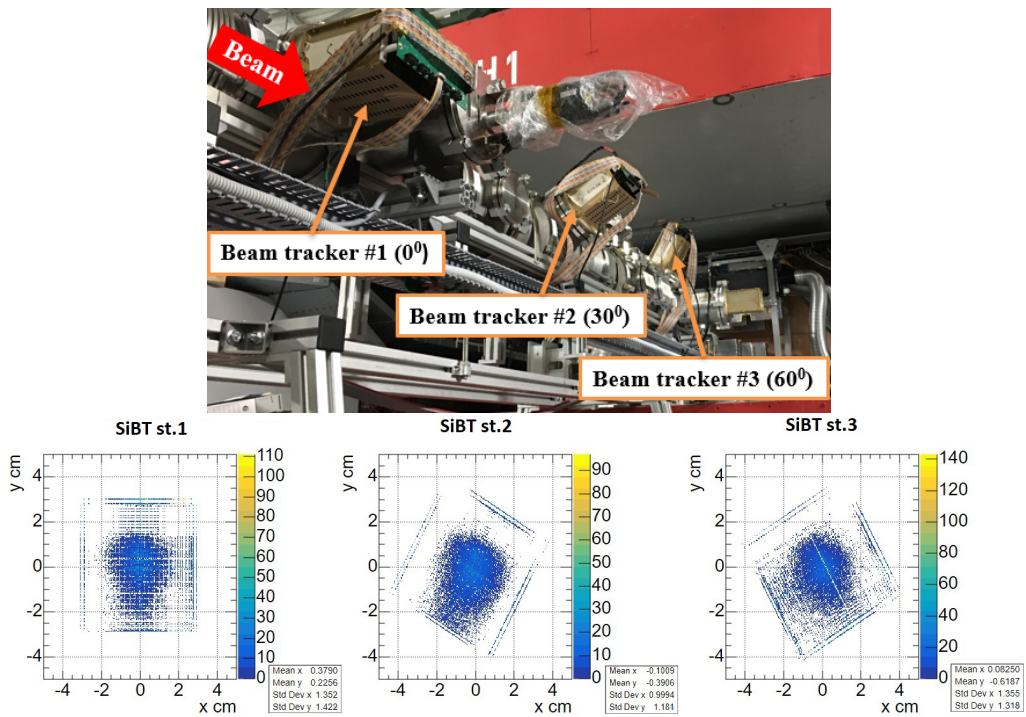


Figure 13: Operating position of three stations of the beam tracker on the vacuum beam pipe of the BM@N channel and two-dimensional beam profiles of Xe ($3.8 \text{ GeV}/n$) nuclei measured by the corresponding BT stations.

276 **5 Central Tracking System.**

277 Central Tracking System (CTS) is based on two large tracking detector systems placed inside the
 278 analysing magnet. These systems are the Forward Silicon Detector (FSD) located right behind the
 279 target area, and a set of Gaseous Electron Multiplier (GEM) detectors installed downstream, inside
 280 the interpole volume. The FSD provides four tracking planes, while the GEM system consists of
 281 seven tracking planes. In order to accommodate the beam vacuum pipe going through the setup,
 282 each tracking plane in both systems is divided in two half-plane detectors, upper and lower.

283 The detectors position and configuration of CTS in the 2023 Xe run is shown in Fig. 14 and
 284 Fig. 15. Detailed description of each tracking subsystem is given in the next sections.

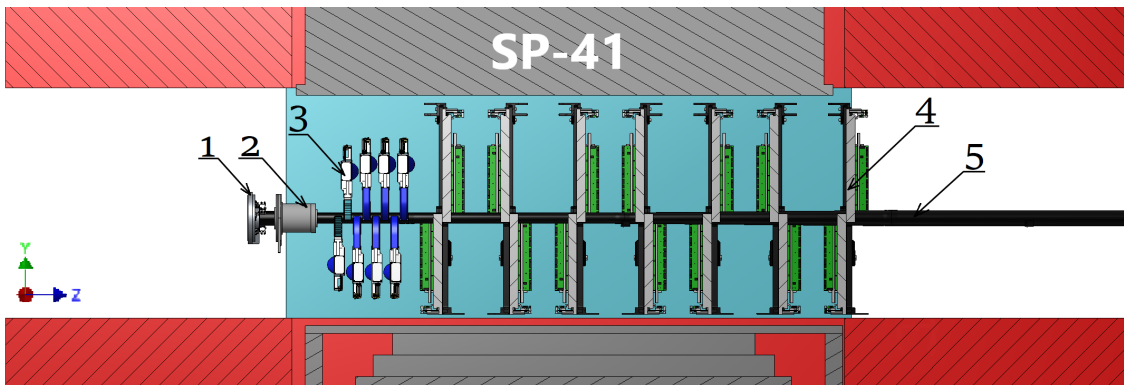


Figure 14: Side view of subsystems inside the analysing magnet: 1) target station, 2) Barrel Detector, 3) Forward Silicon Detector, 4) GEM detectors, 5) beam pipe.

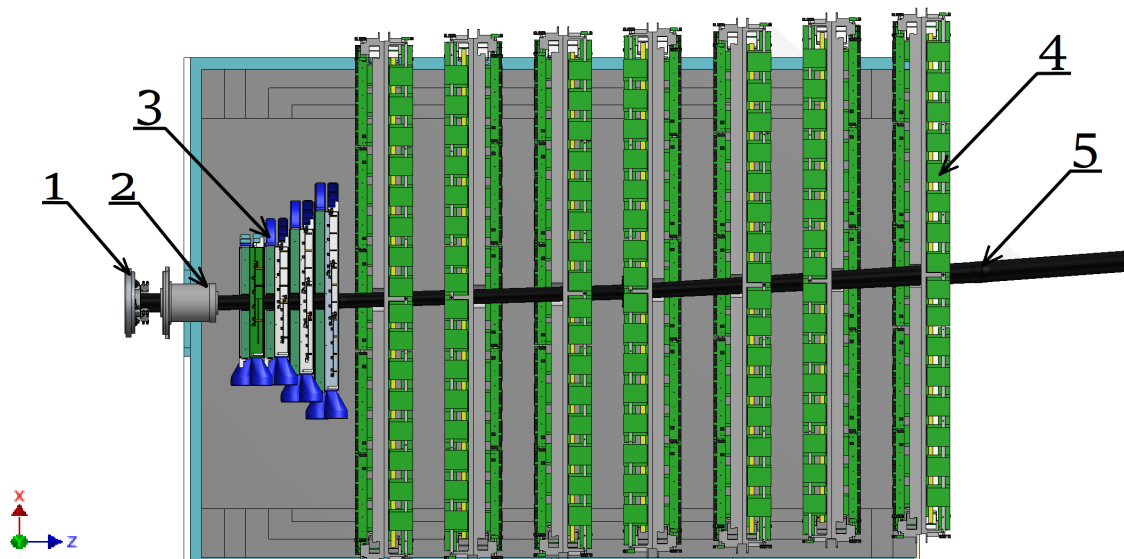


Figure 15: Top view of subsystems inside the analysing magnet: 1) target station, 2) Barrel Detector, 3) Forward Silicon Detector, 4) GEM detectors, 5) beam pipe.

285 **5.1 Forward Silicon Detector**

286 Each half-plane of the FSD forms an independent coordinate detector with the following systems:
 287 coordinate modules based on DSSD, electronics backplane, suspension and precise positioning
 288 mechanics, cable patch panel, air cooling, temperature monitors, light and EM shield. Top and
 289 bottom halves of each plane are made structurally identical and interchangeable. In addition, the
 290 design allows vertical shift of the half-planes during the assembly in order to provide possibility
 291 to mount / dismount the planes regardless of the installed beam pipe and to minimize probability
 292 of its mechanical damage. In the working position, the upper and lower half-planes form a single
 293 coordinate system with active regions overlapping along the Y-coordinate. In the center of each

294 plane there is an insensitive $57 \times 57 \text{ mm}^2$ zone which makes room for the beam pipe. The general
 295 view of the assembled eight half-planes around the beam tube inside the SP-41 magnet is shown
 296 in Fig. 16.

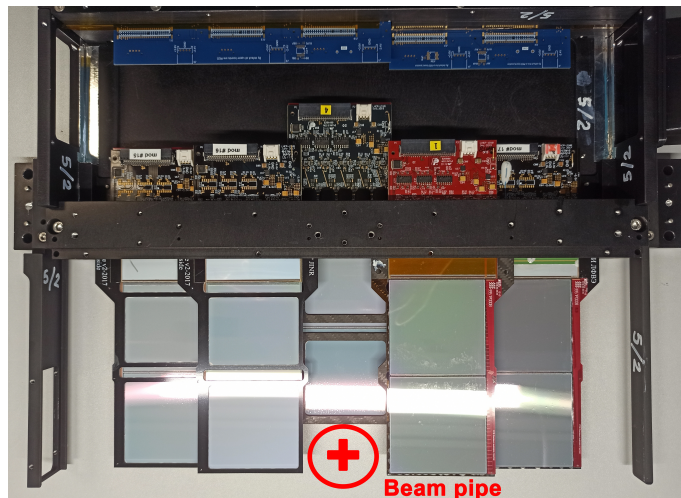


Figure 16: Appearance of the assembled 4 FSD planes (without cables) on the BM@N experiment channel inside the SP-41 analyzing magnet with the beam tube and target assembly installed.

297 The first plane consists of 6 modules each of which uses one DSSD with dimensions of $(93 \times$
 298 $63 \times 0.32) \text{ mm}^2$ positioned in such a way that the long side is aligned with the Y coordinate. The
 299 detector modules of the remaining three coordinate planes use two $(63 \times 63 \times 0.32) \text{ mm}^3$ DSSD
 300 mounted on a common frame with an accuracy of $(\pm 20 \mu\text{m})$, where the strips of the same type of
 301 one DSSD are connected to the strips of another DSSD by ultrasonic bonding (US-bonding) with
 302 an Al-wire $\varnothing 25 \mu\text{m}$. Table 3 provides information about the number of modules and electronic
 303 components in each FSD plane.

Parameters	1st plane	2nd plane	3rd plane	4th plane	Total
Number of Si- modules	6	10	14	18	48
Number of DSSDs	6 $(93 \times 63) \text{ mm}^2$	20 $(63 \times 63) \text{ mm}^2$	28 $(63 \times 63) \text{ mm}^2$	36 $(63 \times 63) \text{ mm}^2$	90
Number of ASICs ($T \leq +25^\circ$)	60	100	140	180	480
Number of PAs	12	20	28	36	96
Number of FEE PCBs	12	20	28	36	96
Number of channels	7680	12800	17920	23040	53760
Area, m^2	0.035	0.073	0.102	0.132	0.307

Table 3: Main parameters of Forward Silicon Detector BM@N

304 The $(63 \times 63 \times 0.32) \text{ mm}^3$ and $(93 \times 63 \times 0.32) \text{ mm}^3$ DSSDs were manufactured at RIMST
 305 (Zelenograd, Russia) and ZNTC (Zelenograd, Russia) respectively. The detectors were cut from 4”
 306 and 6” high-resistivity mono-crystalline silicon wafers produced by the Float Zone method ($\rho > 5$
 307 $\text{k}\Omega \times \text{cm}$). Each side, p^+ and n^+ , contain 640 strips, the strip spacing is 95 and 103 μm , respectively,
 308 and the relative angle between the strips on two sides is 2.5° . The detectors are positioned in such
 309 a way that the strips of the p^+ side are aligned with the Y-axis.

310 Figure 17 shows the external view of the coordinate module with two DSSDs and a demon-
 311 stration of US-bonding. The diagram of the signal input into FEE is presented in Figure 18. The
 312 detector topology (DC) does not contain integrated bias resistors and capacitors for DC decoupling
 313 of the strips from the inputs of the readout electronics. The role of the RC-bias element in the
 314 DC circuit is performed by the integrated Pitch-Adapter (PA), which also performs the matching
 315 of the strip pitch with the pad topology of inputs in the FEE ASIC. Manufactured also at ZNTC,
 316 the PAs were made on the basis of Silicon On Sapphire structure. Each PA has 640 RC channels
 317 with $1 \text{ M}\Omega$ polysilicon bias resistors and $120 \text{ pF}/100 \text{ V}$ integral capacitors. The PA-640 integrated
 318 circuits have low leakage currents (less than 10 $\text{pA}/\text{capacitor}/100 \text{ V}$) and an electrical breakdown
 319 value of 150 V, which corresponds to electric field strength in the capacitor of more than 3 MV/cm .

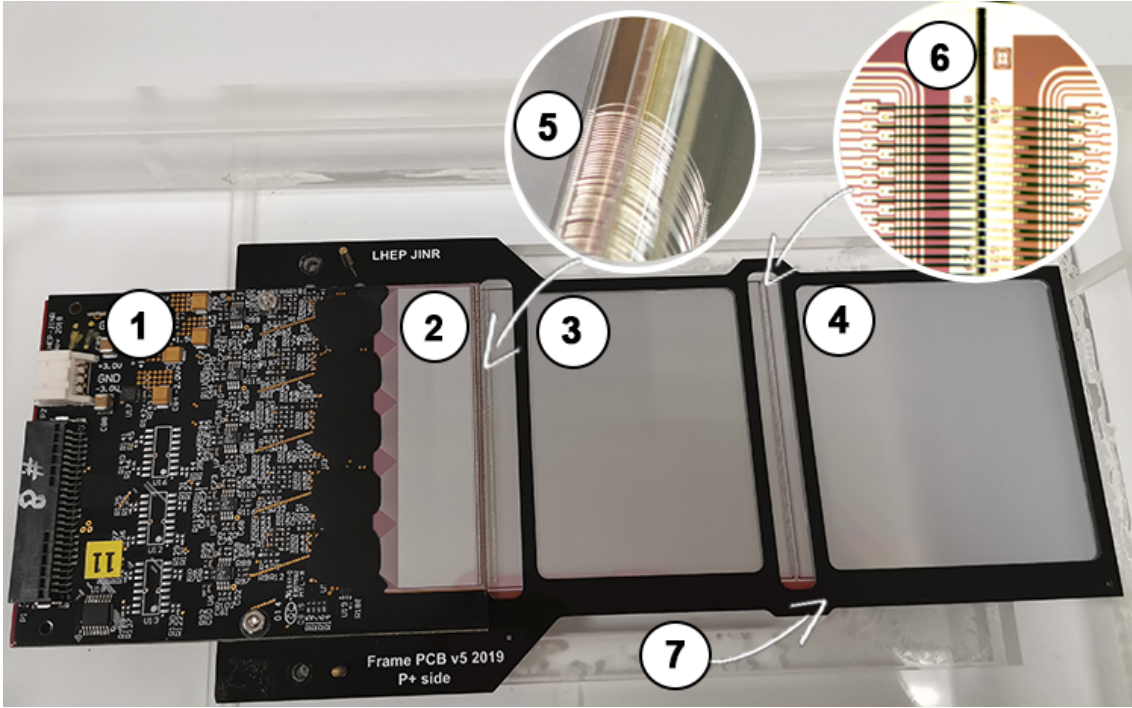


Figure 17: Example on the FSD BM@N coordinate module: 1. Read-out electronics, 2. Pitch Adapter, 3. DSSD1, 4. DSSD2, 5. Example of US - bonding PA + DSSD1, 6. Example of US - bonding DSSD1 + DSSD2, 7. Positioning frame.

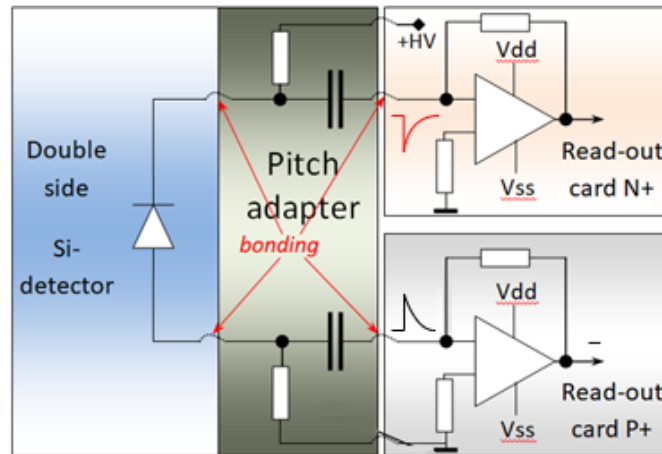


Figure 18: Functional diagram for reading signals from a silicon detector in a coordinate module

320 After passing the PA, the signals from the p^+ and n^+ strips of the detector
 321 of a 128-channel specialized integrated circuit VATAGP7.2 (IDEAS, Norway). Each electronic
 322 registration channel has a charging amplifier ($\sigma - 200 e$), a pulse shaper (peaking time $t_s = 500$
 323 ns), and a memory capacitor which stores pulse amplitude at the trigger time. The ASIC also uses
 324 an analog multiplexer channeling 128 inputs to 1 output sent to the read-out in the DAQ by ADC.
 325 Two printed circuit boards are used in each FSD module in order to accommodate its input signals,
 326 one for 640 negative polarity signals from n^+ strips, the other for 640 positive polarity signals from
 327 p^+ strips. Correspondingly, 5 ASICs are mounted on each PCB, bonding into the pitch adapters
 328 and sealed with a compound.

329 After the assembly of the modules in a half-plane, the position and rotation angles of every
 330 DSSD with respect to geodetic markers on the half-plane housing is measured using the NORGAU
 331 NVM II-5040D video meter with an accuracy of $\pm 5 \mu\text{m}$. The markers are subsequently used
 332 during the installation in order to bind the position of each detector to the common coordinate

333 system of the experimental setup.

334 Fig. 19 illustrates distribution of hits in the 3th plane (7 mod.) of the FSD observed in the
 335 2023 Xe run. Dark bands in the distribution indicate insensitive groups of 128 channels (1 chip).
 336 Number of such faulty chips at the end of the run was equal to 0, 1, 1, 8 for the 1st, 2nd, 3rd
 337 and 4th planes, respectively, which corresponds to 0, 1.0, 0.7 and 4.4 % of the channels. This
 338 malfunction can be due to the following reasons: 1) broken electrical contact in the transmission
 339 circuit from the chip (FEE buffer, cross-board connector, patch panel cable, long ADC-64 cable)
 340 2) failure of the chip (no programming of the operating mode) or breakage of the US-bonding.
 341 Defects of the first type can be repaired, while the failings in the second group are of a permanent
 342 nature.

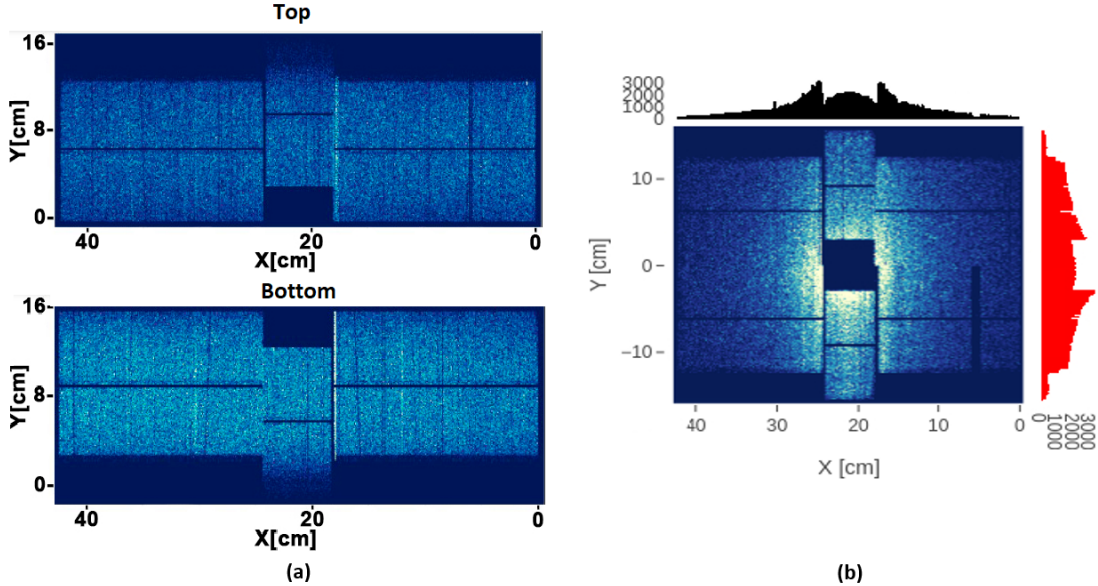


Figure 19: Comparative data on channel occupancy in space tests (a) and in Session BM@N (2022-2023) RUN # 7529 (11.01.2023), $t_c = 25.2^\circ\text{C}$, Target #2 CsI (2%) (b).

343 5.2 GEM

344 Triple-GEM detectors located inside the analysing magnet SP-41 downstream the FSD. Full con-
 345 figuration of the GEM tracking system implemented in the 2023 Xe run consists of 14 detectors
 346 forming 7 tracking planes: 7 top detectors above the vacuum beam pipe, and 7 bottom detectors
 347 below the pipe. Because the beam line inside the SP-41 goes closer to the bottom pole of the
 348 magnet, in order to cover the maximum possible acceptance, the top and bottom detectors have
 349 been designed with different active area sizes, $163 \times 45 \text{ cm}^2$ and $163 \times 39 \text{ cm}^2$, respectively.

350 5.2.1 GEM construction

351 The BM@N GEM detectors were produced using non-glue "foil-stretching" technology and assem-
 352 bled at CERN in the PH Detector Technologies and Micro-Pattern Technologies workshop. All
 353 three GEM foils in a detector are identical and made of a $50 \mu\text{m}$ Kapton covered on both sides
 354 with $5 \mu\text{m}$ copper electrodes. Foils are perforated by holes of about $70 \mu\text{m}$ diameter, separated by
 355 a distance of $140 \mu\text{m}$. The gaps between the electrodes are shown in Fig. 20 (left).

356 The anode plane is used for the readout and organized as a multilayered board with two types of
 357 parallel strips: aligned with the vertical axis and inclined by 15 degrees with respect to it, as shown
 358 in Fig. 20 (right). The width of vertical and inclined strips is $680 \mu\text{m}$ and $160 \mu\text{m}$ respectively,
 359 while the pitch for both types of strips is $800 \mu\text{m}$. The readout plane is subdivided by two halves
 360 and, in addition, separate readout is organized for the region close to the beam pipe where higher
 361 density of hits is expected. The size of this "hot zone" is approximately $80 \times 15 \text{ cm}^2$. The readout
 362 FEE boards are mounted on the frames of the detectors outside of the acceptance. More details
 363 on the design, tests and preparation of the detectors can be found in [13, 14].

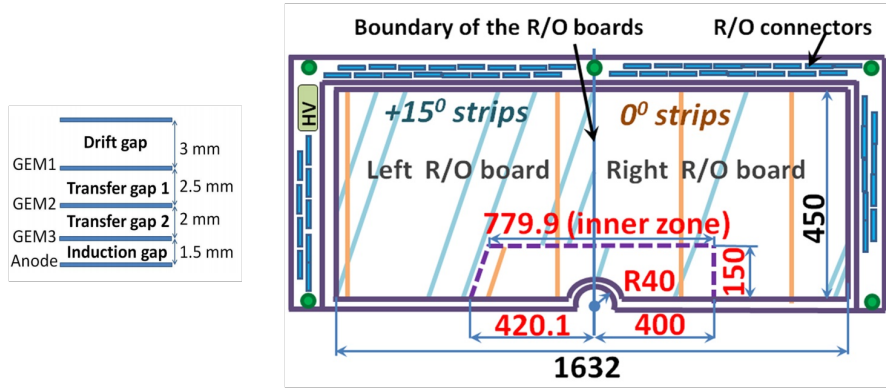


Figure 20: Design of the detectors: cross-section of triple GEM (left); schematic view of the top detector (right).

364 **5.2.2 Mechanical support**

365 The mechanical support of the GEM detectors inside the SP-41 magnet was designed and man-
 366 ufactured by LLC “Pelcom Dubna Machine-Building Plant”. The support structure is made of
 367 non-magnetic material and satisfies strict requirements for precise positioning of the detectors.
 368 The weight of one GEM detector equipped with mechanics, front-end electronics and cables is
 about 19.5 kg. The whole assembly of 14 GEM detectors during the installation can be vertically

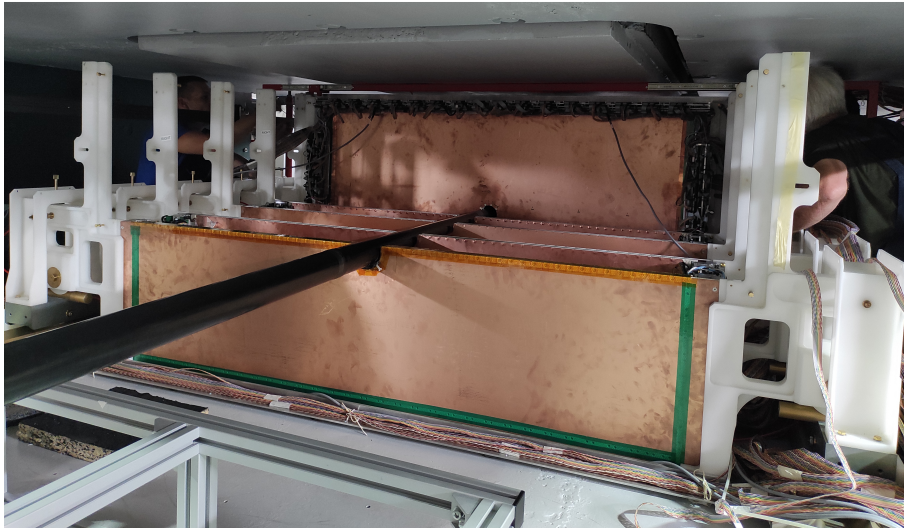


Figure 21: Photo of GEM detectors installation from back side of SP-41 magnet (in the direction opposite to the beam)

369 adjusted by ± 10 mm relative to the surface of the magnet coil. In addition, the setup allows to shift
 370 each GEM detector vertically by ± 5 mm with respect to the mechanical support. The accuracy of
 371 positioning of each detector relative to the other (one half-plane relative to the other half-plane ?)
 372 does not not exceed 0.5 mm. After the installation and alignment of each detector, the coordinates
 373 of the frame corners and the center of the semi-circular notch for the beam pipe are measured with
 374 an accuracy better than xxx.

375 Installation of the detectors includes the following steps: 1) bottom detectors are installed

377 sequentially, starting from the detector closest to the target; 2) a carbon beam pipe is installed on
378 top of the bottom detectors; 3) top detectors are installed sequentially, starting from the detector
379 closest to the target. Photo of the installation process is shown in Fig. 21.

380 Prior to the installation the detectors were tested with cosmic muons in order to determine
381 uniformity of the gain in different regions. Lower amplification in the outer parts of the detectors
382 was observed, with typical variation in the range $\pm 20\%$. During the installation, the detectors,
383 which, due to this effect, can have lower efficiency in the side parts, were placed closer to the target,
384 where outer regions are less significant for track reconstruction.

385 5.2.3 Gas system

386 Ar(80)C₄H₁₀(20) gas mixture was chosen for the operation in the 2023 Xe run, while the overall
387 GEM amplification was maintained at the level of 3×10^4 . The H₂O and O₂ removal filter was
388 installed in the gas system after the gas mixer. The gas line is divided into two identical lines for
389 independent connection of the top and bottom GEM detectors. Two rotameters were installed in
390 the lines, allowing to regulate the gas flow. Each line connected a group of top or bottom detectors
391 in series, starting with the detector closest to the target. The small GEM detector (see the section
392 "Beam and trigger detectors") was connected last in the line for the bottom detectors. The gas
393 flow rate in each line during the 2023 Xe run was at the level of 3 l/h.

394 5.2.4 Front-end electronics

395 Front-end electronics is based on the 32-channel integrated circuit VA163 (IDEAS, Norway). Each
396 channel of the ASIC has a charge sensitive pre-amplifier, a shaper with 2 μ s peaking time, and
397 a sample holder circuit. An analog multiplexer sends channel by channel 32 sampled signals into
398 one serial read-out. Four ASICs are joined in one front-end board. The multiplexed data from
399 each board are transmitted through 13m of twisted pair flat cable to the 12-bit analog-to-digital
400 converter. More detailed description of the FEE can be found in [15].

6 TOF

(*RumyantsevM.mikhail.rumyantsev@yandex.ru*)

For charge particle identification the two Time-of-flight systems are used in BM@N. The first TOF system is placed at about 4 meters from the target and looks like two arms to the left and right of beam axis (TOF-400). The second TOF wall (TOF-700) is located at a distance of 7 meters from the target (fig 1). The arrangement of both systems provides continuous geometric acceptance and overlap with the external track systems. The basic requirements to the TOF system are:

- high granularity to keep the overall system occupancy below 15% and minimize efficiency degradation due to double hits;
- good position resolution to provide effective matching of TOF hits with tracks;
- high combined geometrical and detection efficiency (better than 85%);
- identification of pions and kaons with $0.1 < p_t < 3$ GeV/c;
- identification of (anti)protons with $0.3 < p_t < 5$ GeV/c

To achieve these goals, a strip-readable Multigap Resistive Plate Chamber (MRPC) detector was chosen for both TOF systems. This type of detectors is widely used for time-of-flight measurements (ref...). It showed good efficiency, high time resolution, the ability to work with particles flux up to tens kHz/cm².

6.1 TOF400

The TOF400 system consists of two part are placed left and right to the beam. Every part consist of two gas boxes (modules) with 5 MRPCs each 22. The active area of the MRPCs overlap on 50 mm inside the box. Gas box made from aluminum frame covered by aluminum honeycomb for reduction of radiation length. Overlap of gas boxes ensures crossing of active area of detectors 50 mm also. Active area of every part is 1.10x1.3 m² and defined to satisfy the geometrical acceptance of the GEM tracking detectors. The main parameters of the TOF400 are present in Table 5.

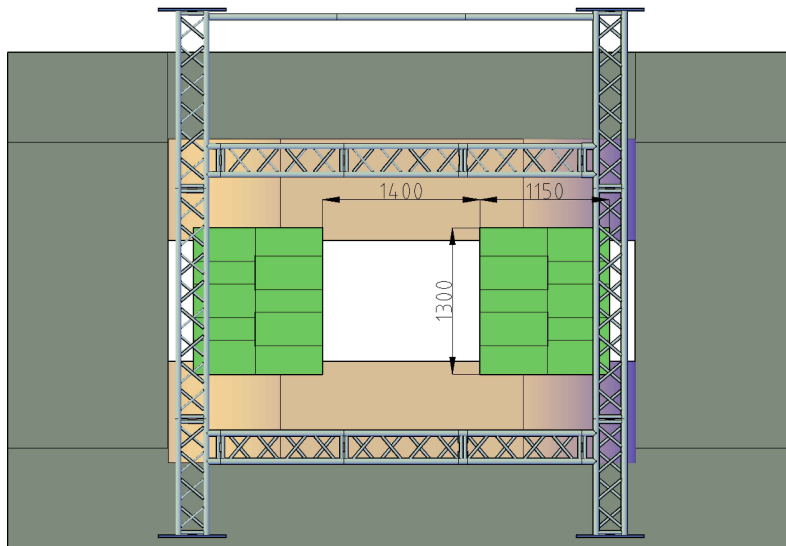


Figure 22: Schematic view of TOF400 system

A scheme of MRPC for TOF400 system is shown on Fig. 28. The detector consists of three stacks of 5 gas gaps each. Float glass with a thickness of 420 μm for external electrodes of the stack and 240 μm for internal ones was used as resistive electrodes. The fishing line as a spacer defines the 200 μm gap between all resistive electrodes. The outer part of external glass electrodes is covered by conductive paint with surface resistivity about 2-10 $\text{M}\Omega/\square$ to apply high voltage. All internal glasses are floating. The pickup electrodes look like strips and made on the PCB board. The main feature of the proposed triple-stack MRPC is that readout strips are located only in the

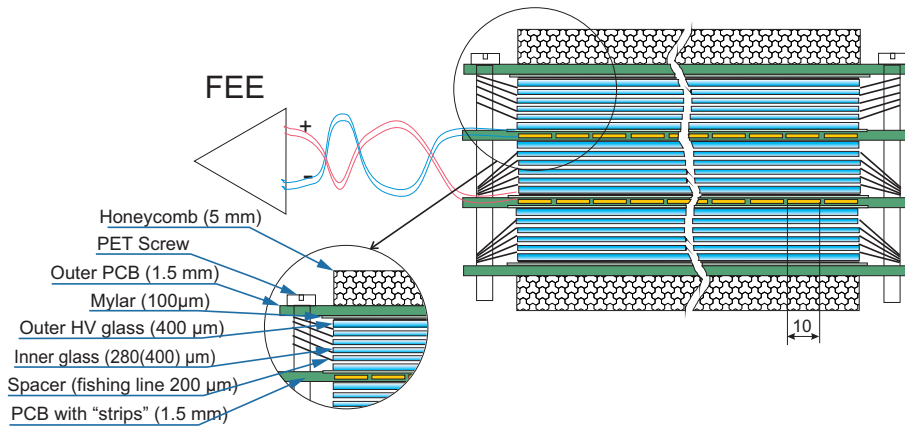


Figure 23: Schematic view of the MRPC detector for TOF400 system

432 inner stack. This ensures that the construction is symmetric, and speed of signals on the anode
 433 and cathode are the same, what prevent the dispersion of the signal. Differential analog signal
 434 from strip is transferred by twisted pair cable to front-end electronics. Signal is reading out from
 435 both ends of the strip. It provides better time resolution and determination of the coordinate of a
 436 particle along the strip. For stiffening structure we glue paper honeycomb with a thickness of 10
 437 mm on outer part of the external PCBs. Dimension of active area of one MRPC is 300*600 mm².
 438 It has 48 readout strips, 10 mm wide and 300 mm long. To reduce crosstalk the gap between strips
 439 is 2.5 mm. Thus the pitch of electrodes in this case is 12.5 mm.

440 The charge sensitive NINO chip was used for TOF400 [1]. The chip has 8 channels and processed
 441 on 0.25 μm technology. Each channel includes ultra-fast preamplifier with a peaking time less
 442 than 1 ns, discriminator with a minimum detection threshold of 10 fC and output stage which
 443 provides LVDS output signal. The duration of the LVDS signal is proportional to the charge
 444 of the input signal, so it can be used for so-called amplitude-time correction. The 24-channel
 445 amplifier-discriminator base on NINO chip was developed in LHEP JINR [2]. Measurements with
 446 a test signal from the generator showed an intrinsic time resolution of the amplifier of 7 ps. The
 447 amplifier are placed as close to the MRPC as possible on front cover of the gas box. The signal
 448 from the preamplifier can be transmitted over a distance of up to 10 m via a special cable without
 449 loss of time resolution. Additional features of the FEE are the ability to remotely control the
 450 threshold, measure the supply voltage and temperature on the board via the RS485 interface.

451 72-channel time-to-digital converters (TDC72VHL [3]) based on HPTDC chip [4] were developed
 452 in LHEP JINR for digitization of LVDS signals and data acquisition. The TDC72VHL operates in
 453 ultra high resolution mode with a binning of 23.4 ps. This allows to measure the leading and trailing
 454 edges of the input LVDS signal with high accuracy, but there is significant integral non-linearity at
 455 the TDC. This nonlinearity causes strong degradation of time resolution. The method of uniform
 456 filling the time gap with random events (code density test) was used for calibration (consideration
 457 of nonlinearity) of TDC module. The intrinsic time resolution of an individual TDC72VHL channel
 458 averaged 20 ps after applying the calibrations.

459 The prototype of full scale MRPC with full readout chain was tested on the Nuclotron beam
 460 at LHEP. The deuteron beam was transferred to the experimental setup “Test MPD” [5]. The fast
 461 Cherenkov counter [6] with time resolution of 37 ps was used as a start detector. The result of
 462 measuring the efficiency and time resolution are present on the Fig. 29a . All results include
 463 contributions from the front end and data acquisition electronics. The efficiency is higher than
 464 98% and time resolution is below 50 ps for different threshold of NINO. A voltage of 11.5 kV and a
 465 threshold of 120 mV were chosen as the operating point. Results of high rate test are presented on
 466 Fig. 29b. MC simulations show that the particle flux on the TOF400 does not exceed 1 kHz/cm²,
 467 so a time resolution of less than 50 ps and an efficiency of more than 95% are expected.

468 6.2 TOF700

469 The TOF700 wall placed at about 7 meters from the target and made of MRPC of different size
 470 in an individual gas box each. The wall size of 3.2x2.2 m² is defined to satisfy the geometrical
 471 acceptance of the outer tracking detectors (DCH). The detectors are mounted on two subwalls in
 472 two layers on each to provide a geometric overlap between the detectors. Both sub walls can move
 473 relative to each other to provide access for installation and maintenance. Two types of detectors

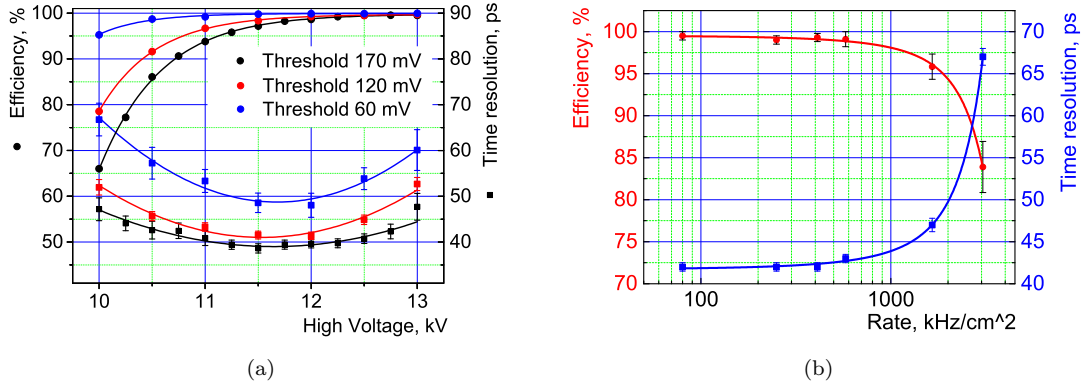


Figure 24: Performance of the MRPC designed for TOF400 system. The detector efficiency and time resolution as function of applied of HV for different NINO thresholds are shown on the left. The right shows the dependence of the detector performance on the particle flux for 11.5 kV and 120 mV threshold.

474 are used for TOF700: a "cold" MRPC with an active area of $30.3 \times 56 \text{ cm}^2$ (16 strips of 18×560
 475 mm^2) for the area with a low particle flux and a "warm" MRPC with an active area of 16×35.1
 476 cm^2 (32 strips $10 \times 160 \text{ mm}^2$) for the area near the beam line. The main parameters of the TOF700
 477 are present in Table 5.

478 A schematic cross-section of a "cold" MRPC is shown in Fig. 31. It consists of two identical
 479 stacks with five gaps each. Each stack is formed by six glass plates 0.67 mm thick with the bulk
 480 resistivity of $2 \times 10^{12} \Omega \times \text{cm}$. The gap between the glasses 0.3 mm is fixed by spacers (fishing-lines).
 481 Graphite conductive coating with surface resistivity of $1 \text{ M}\Omega/\square$ is painted to outer surfaces of
 482 external glass plates to distribute both the high voltage and its ground. The anode readout plate
 483 is a $100 \mu\text{m}$ one-sided printed PCB and is placed between stacks. Unipolar signals are taken
 484 from both ends of the reading strips, which makes it possible to determine the coordinate of the
 485 particle along the strip. Each detector is placed in an individual gas box. The bottom cover is
 486 made of PCB 2.5 mm thick and is designed to take out a signal from the box volume to readout
 487 electronics. The frame of the box is made of aluminum 2.5 mm thick. The top cover is made of 1.5
 488 mm thick aluminum sheet. The box covers are reference plan for a unipolar signal. Warm MRPC
 489 is built in the same way as cold MRPC. However to increase the rate capability the gas gaps and
 490 the thickness of the glass plates are reduced (0.22 mm and 0.55 mm respectively). To compensate
 491 for the loss of the signal amplitude due to the increasing of the anode strip-cathode capacity, the
 492 number of gaps in the chamber was increased from 10 to 12 (six gaps per stack).

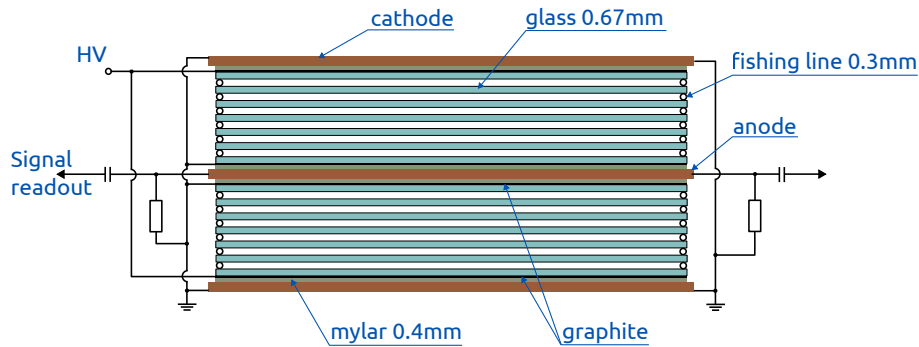


Figure 25: Schematic view of the MRPC detector for TOF700 system

493 The AddOn board base on NINO chip developed for the HADES experiment was chosen as
 494 front-end electronics (FEE) for TOF700. Signals from the MRPC to the FEE (32RPC) are received
 495 over 50 ohm coaxial cables using MMCX connectors. The LVDS output signals are transmitted
 496 to the digitizing module using DHR-78F connectors. A 64-channel VME TDC64VHLE time-
 497 to-digital converter based on the HPTDC chip is used for digitization. With a special module
 498 (PWR&CTRL) it is possible to remotely control the power supply, the discrimination threshold
 499 and hysteresis value on the FEE.

500 Prototypes of "cold" and "warm" detectors were tested on the secondary muon beam of the
 501 U-70 accelerator at IHEP. The test was carried out on the "MUON" facility with a particle flux
 502 of about 1 kHz/cm². A fast scintillation counter with its own time resolution of 40 ps was used as
 503 T0. The test results of both prototypes are shown in the figure 32. The intrinsic time resolution
 504 of the MRPCs with electronics is better than 45 ps with an efficiency of 98% and 95% for "cold"
 505 and "warm" chambers respectively.

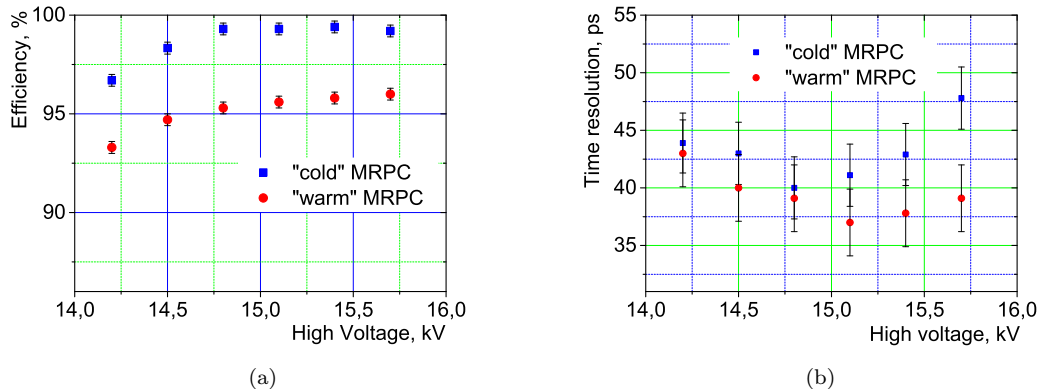


Figure 26: Performance of the MRPC designed for TOF700 system. The detectors efficiency are shown on the left and time resolution are shown on the right.

	TOF400	TOF700
MRPC active area	30x60 cm ²	30.3x56 cm ² "cold" 16x35.1 cm ² "warm"
FEE on one MRPC	96	32 for "cold" 64 for "warm"
Number of MRPC	20	30 "cold" 40 "warm"
Total active area	2 Arms x 1.1x1.3 m ²	3.2x2.2 m ²
Total number of FEE	1920	3520

Table 4: Main parameters of TOF system.

506 6.3 Services system

507 Both TOF400 and TOF700 systems use the same a non-flammable Freon rich gas mixture contain-
 508 ing 90% C₂H₂F₄ + 5% i-C₄H₁₀ + 5% SF₆. A simple open-loop gas system was designed for the
 509 BMN experiment. This system is based on the MKS 1479A controllers for measuring and adjusting
 510 the absolute flow of components with an accuracy of 0.3%. The flow rate of the gas mixture can
 511 be adjusted in the range from 6 l/h to 90 l/h, but the typical value is 21 l/h, which corresponds
 512 to the exchange of 2 volumes per day. Also, one additional channel is available for purging the
 513 system with nitrogen for cleaning and drying. A special PC program has been written to control
 514 the parameters of the gas system via the Ethernet interface.

515 The MRPC detector operates at very high voltage of 12 kV and 15 kV for TOF400 and TOF700
 516 respectively. On the other hand, the dark currents of the detector are quite small at the level of
 517 tens of nA. Also, the detector is very sensitive to voltage ripples due to the large capacitive coupling
 518 between the high-voltage layer and the readout strips. Therefore, the high-voltage system is subject
 519 to high requirements for voltage stability and current measurement accuracy. The high-voltage
 520 power supply systems for both TOF are based on commercially available ISeg modules and a
 521 specially designed HVSys power supply. All elements of the system have the ability to remotely
 522 control via Ethernet interface.

523 To monitor of stability of operation of the TOF systems all controlled parameters are sent to
 524 the Slow Control System. The data is displayed on the website of the experiment via Grafana.
 525 The operator can see the value of the high voltage and current on the detectors, the set voltages

526 and thresholds of the amplifiers, the gas flow and the weight of the gas in cylinders, and other
527 parameters. In case of an emergency, the operator receives a message that allows to respond in
528 time. All data is stored in a database and can be used for further analysis.

529 7 TOF v2

530 Two time-of-flight systems are used in BM@N for charge particle identification. The first system,
 531 TOF-400, is placed at about 4 meters from the target and consists of two arms to the left and
 532 right of the beam axis. The second, TOF-700, is located at a distance of about 7 meters from the
 533 target. The arrangement of both systems provides continuous geometric acceptance and overlap
 534 with the FSD, GEM and outer tracking systems. Choice of detectors and their parameters was
 535 dictated by the following requirements:

- 536 - high granularity and rate capability, which would allow to keep the overall system occupancy
 537 below 15% and minimize efficiency degradation due to double hits;
- 538 - good position resolution in order to provide effective matching of TOF hits with tracks;
- 539 - high combined geometrical and detection efficiency (better than 85%);
- 540 - separation of pions and kaons in the momentum range $0.1 < p < 3$ GeV/c;
- 541 - separation of kaons and protons in the momentum range $0.3 < p < 5$ GeV/c.

542 To achieve necessary performance, a strip-readable Multigap Resistive Plate Chamber (MRPC)
 543 detector was chosen for both TOF sub-systems. This type of detectors is widely used for time-
 544 of-flight measurements. It showed good efficiency, excellent time resolution, ability to work with
 545 particle flux up to tens kHz/cm².

546 7.1 TOF400

547 Left and right arms of the TOF400 system are placed symmetrically with respect to the beam.
 548 Every part consists of two gas boxes (modules) each having 5 MRPC detectors [27](#). The active area
 549 of one detector is 60x30 cm². Inside the box, active areas of adjacent detectors overlap vertically
 550 by 50 mm, while horizontal overlap of the gas boxes ensures crossing of active area of detectors by
 551 50 mm as well, which makes total active area of each of the two arms to be equal to 1.10x1.3 m²
 552 matching the geometrical acceptance of the 1x1 m² CSC tracking detectors and covering significant
 553 fraction of the GEM acceptance. Each gas box is formed by an aluminum frame closed from the
 554 front and back sides by aluminum honeycomb plates, which provide sufficient rigidity while having
 555 small thickness in radiation lengths.

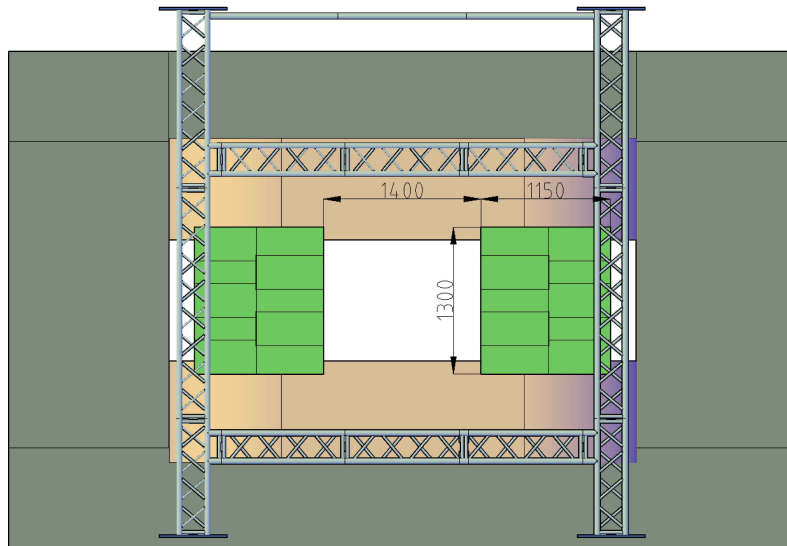


Figure 27: Schematic view of TOF400 system

556 Fig. [28](#) shows schematic cross section of the TOF400 MRPC. The detector consists of three
 557 stacks inserted between two outer 1.5 mm thick PCBs, and separated by two inner PCBs also
 558 1.5 mm thick. In order to add stiffness to the structure, paper honeycombs with a thickness of
 559 10 mm were glued on the outer sides of the external PCBs. Each stack has 5 gas gaps between

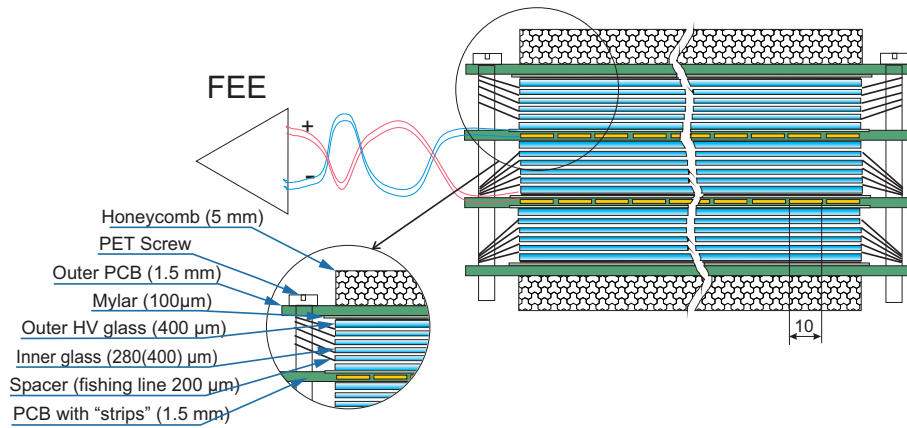


Figure 28: Schematic cross section of TOF400 MRPC

560 glass sheets which are used as resistive electrodes. Two external glass sheets in a stack have a
 561 thickness of $420\ \mu\text{m}$, while four internal sheets are $240\ \mu\text{m}$ thick (the numbers in the Figure are
 562 different Sic!). Fishing line as a spacer defines the $200\ \mu\text{m}$ gap between all the glass plates. High
 563 voltage is applied to the outer part of external glass electrodes covered by conductive paint with
 564 surface resistivity of about $2\text{-}10\ \text{M}\Omega/\text{sq}$. All internal glass electrodes are left electrically floating.
 565 Two PCBs with pickup readout pads are placed on both sides of the inner stack, one serving as
 566 the cathode readout plane, the other as the anode one. Correspondingly, the HV is applied in an
 567 alternating sequence, as shown on the right side of the Fig. 28, (***) should be added to the picture!
 568 (***) in order to form symmetrical configuration for the cathode and anode readout planes. Such
 569 a configuration was chosen to ensure that propagation of signals to the FEE has equal speed on
 570 positive and negative lines, thus preventing dispersion of the differential signal.

571 Readout pads have a shape of strips with area of $300\times 10\ \text{mm}^2$ arranged vertically with 12.5
 572 mm pitch, making 48 readout strips in each of the PCBs. The $2.5\ \text{mm}$ gap between the strips
 573 is introduced in order to reduce cross talk between adjacent channels. Signals from strips are
 574 transferred to the front-end electronics by twisted pair cables. In order to obtain better time
 575 resolution and determination of hit coordinate along the strip, the signals are read out from both
 576 ends of the strip.

577 FEE of the TOF400 is based on the NINO amplifier/discriminator ASIC developed in CERN
 578 for the time-of-flight system of the ALICE experiment [?]. The chip has 8 input channels and
 579 processed on $0.25\ \mu\text{m}$ technology. Each channel includes an ultra-fast preamplifier with peaking
 580 time less than $1\ \text{ns}$, a discriminator with a minimum detection threshold of $10\ \text{fC}$ and an output
 581 stage which provides LVDS output signal. The duration of the LVDS signal is proportional to the
 582 charge of the input signal, and can be used for the amplitude-time correction. The 24-channel
 583 FEE board, which combines signal processing by three NINO chips, was developed in LHEP JINR
 584 [?]. In order to ensure optimal operation of the FEE, the boards are placed as close to the MRPC
 585 as possible and mounted on the front cover of the gas box. Measurements with a test signal from
 586 the generator showed an intrinsic time resolution of the FEE chain of about $7\ \text{ps}$. Additional
 587 features of the FEE board include the ability to remotely control the threshold levels of the NINO
 588 discriminators, and to measure the supply voltage and temperature on the board via the RS485
 589 interface.

590 LVDS signals from the FEE boards are transmitted over a distance of up to $10\ \text{m}$ via a special
 591 cable without loss of time resolution. The signals are digitized in 72-channel time-to-digital con-
 592 verters (TDC72VHL) based on the HPTDC chip [?]. The TDC72VHL were developed in LHEP
 593 JINR and operate in ultra high resolution mode with a binning of $23.4\ \text{ps}$ [?]. Such fine binning
 594 allows to determine the leading and trailing edges of the input LVDS signals with high accuracy.
 595 However, the TDCs exhibit significant integral non-linearity, which, if not corrected, causes signifi-
 596 cant degradation of the time resolution. The method of uniform filling the TDC time window with
 597 random events (code density test) is used for non-linearity calibration of every channel of the TDC
 598 module. After applying the non-linearity correction, the intrinsic time resolution of individual
 599 TDC72VHL channels is equal to $20\ \text{ps}$ on average.

600 A full scale MRPC prototype with complete readout chain and $90\% \text{C}_2\text{H}_2\text{F}_4 + 5\% \text{i-C}_4\text{H}_{10} +$
 601 $5\% \text{SF}_6$ gas mixture was tested in the Nuclotron deuteron beam [?]. Fast Cherenkov counter with
 602 time resolution of $37\ \text{ps}$ was used as a start detector. Measured efficiency and time resolution as a
 603 function of high voltage for different levels of the NINO discriminator threshold are presented in the

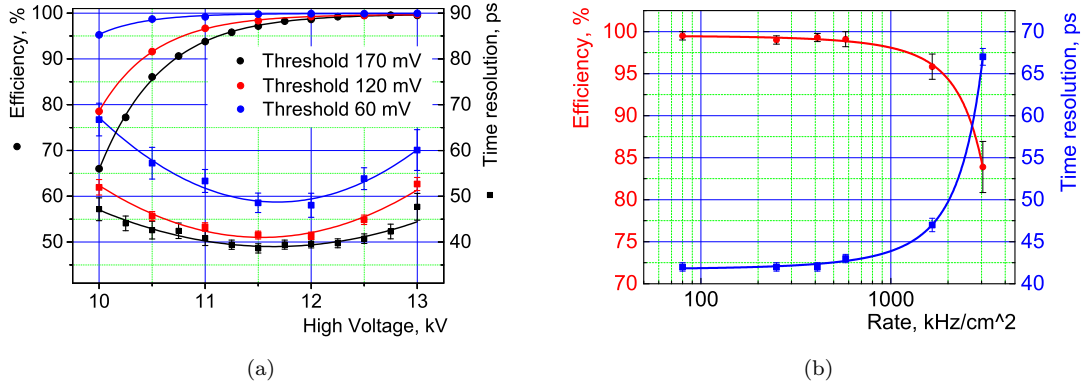


Figure 29: Performance of the MRPC designed for TOF400 system. The detector efficiency and time resolution as a function of applied of HV for different NINO thresholds are shown on the left. The right plot shows the dependence of the detector performance on the particle flux for 11.5 kV and 120 mv threshold.

604 Fig. 29a. All the results include contributions from the front-end and data acquisition electronics.
 605 Based on the measured prototype performance, high voltage of 11.5 kV and discriminator threshold
 606 of 120 mV were chosen as the operating point of the TOF400 modules. With these settings, the
 607 dependence of efficiency and time resolution on the particle rate was studied with the prototype,
 608 the results of these tests are presented in Fig. 29b. Monte Carlo simulations show that under the
 609 BM@N conditions, even at the highest heavy ion beam intensity, the particle flux in the TOF400
 610 does not exceed 1 kHz/cm², therefore, time resolution better than 50 ps and efficiency higher than
 611 95% are expected.

612 7.2 TOF700

613 The TOF700 wall is placed at about 7 meters from the target and has active area of 3.2x2.2
 614 m² in X and Y, respectively, defined to overlap with the geometrical acceptance of the outer
 615 tracking detectors (DCH and 2.2x1.5 m² CSC) as well as to cover significant fraction of the GEM
 616 acceptance. At the center of the TOF700 wall there is an opening for the vacuum beam pipe.
 617 Because density of hits from particles produces in heavy ion collisions significantly higher in the
 618 region close to the beam, two types of MRPC detectors are used for TOF700: "cold" – with an
 619 active area of 30.3x56 cm² and 16 readout strips of 18x560 mm² for the outer area with a low
 620 particle flux, and "warm" – with an active area of 16x35.1 cm² and 32 strips of 10x160 mm² for
 621 the area near the beam line. Vertical orientation and the size of the readout strips were dictated
 622 by expected hit occupancy and the requirement of unambiguous matching of hits with particle
 623 tracks. Arrangement of TOF700 MRPCs in the XY plane is shown in 30. The detectors are
 624 mounted on two sub-walls, which can slide relative to each other to facilitate access for installation
 625 and maintenance of the detectors. In addition, the MRPCs in each sub-wall are arranged in two
 626 layers in order to provide possibility for geometrical overlap between adjacent detectors.

627 "Cold" and "warm" MRPCs have similar two-stack design with a single anode readout plane
 628 placed between the stacks. A schematic cross-section of a "cold" MRPC is shown in Fig. 31.
 629 Each stack is formed by six glass plates 0.67 mm thick with the bulk resistivity of $2 \times 10^{12} \Omega \times \text{cm}$.
 630 Fishing-lines spacers define 0.3 mm gap between the glass sheets. Graphite conductive coating
 631 with surface resistivity of 1 M Ω /sq is painted on the outer surfaces of the external glass plates
 632 in order to apply both the high voltage and the ground. The anode readout plane is arranged
 633 on a 100 μm one-sided PCB. Unipolar signals are taken from both ends of the strips, which
 634 makes it possible to determine the coordinate of the particle hit along the strip by measuring time
 635 difference between the signals. Each detector is placed in an individual gas box, which is formed
 636 by a 2.5 mm thick aluminum frame and two cover plates. One cover is made of 2.5 mm thick PCB
 637 and is designed to take out signal wires from the box volume to the readout electronics. The other
 638 cover is made of 1.5 mm thick aluminum sheet.

639 The design of "warm" MRPCs has only minor modifications. In order to increase detectors
 640 rate capability, the gas gaps and thickness of the glass plates in warm MRPCs are reduced to 0.22
 641 mm and 0.55 mm respectively. Such a reduction leads to lower signal amplitudes due to increased

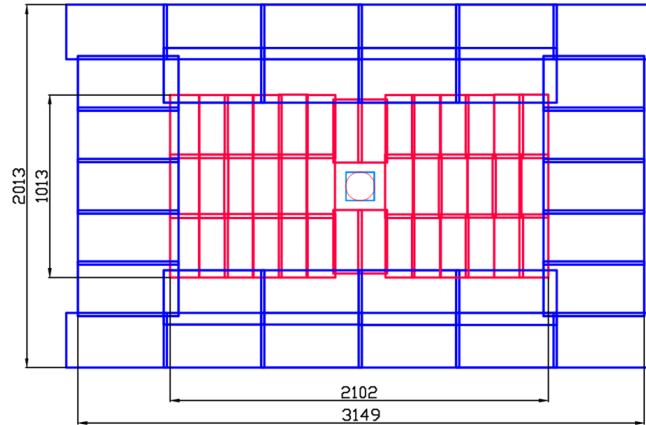


Figure 30: Arrangement 40 "warm" (red) and 32 "cold" (blue) MRPCs in the TOF700 active area.

642 anode strip-cathode capacity. To compensate for this signal weakening, the number of gaps in the
 643 chamber was increased from 10 to 12 (six gaps per stack).

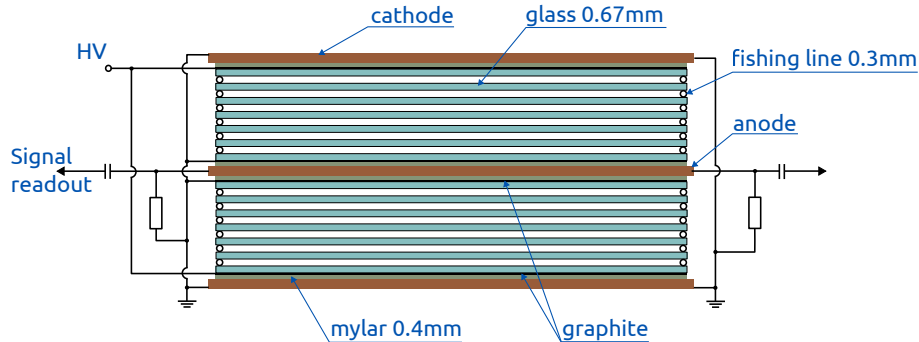


Figure 31: Schematic view of the MRPC detector for TOF700 system

644 The FEE board developed for the HADES experiment was chosen as front-end electronics
 645 for the TOF700. Signals from the MRPC are sent to the FEE over 50 ohm coaxial cables with
 646 MMCX connectors. The boards are based on the NINO ASICs, which, as already mentioned,
 647 process the signals in such a way that the duration of the LVDS output signals is proportional to the
 648 amplitude of the input signals, suitable for implementation of the time-over-threshold method. The
 649 output signals are transmitted to the digitizing module using DHR-78F connectors. A 64-channel
 650 VME TDC64VHLE time-to-digital converter based on the HPTDC chip is used for digitization.
 651 With a special module (PWR&CTRL) it is possible to remotely control the power supply, the
 652 discrimination threshold and hysteresis value in the FEE boards.

653 Prototypes of "cold" and "warm" TOF700 detectors were tested in the secondary muon beam
 654 of the U-70 accelerator at IHEP (Protvino, Russia). The test was carried out at the "MUON"
 655 facility with a particle flux of about 1 kHz/cm². A fast scintillation counter with its own time
 656 resolution of 40 ps was used as a start counter. The test results of both prototypes are shown in
 657 the figure 32. The intrinsic time resolution of the MRPCs with electronics is better than 45 ps
 658 with an efficiency of 98% and 95% for "cold" and "warm" chambers respectively.

659 Main parameters of the TOF400 and TOF700 sub-systems are summarized in Table 5.

660 7.3 Services system

661 Both TOF400 and TOF700 systems use the same a non-flammable Freon rich gas mixture con-
 662 taining 90% C₂H₂F₄ + 5% i-C₄H₁₀ + 5% SF₆. A simple open-loop gas system was designed for
 663 the BM@N experiment. This system is based on the MKS 1479A controllers for measuring and
 664 adjusting the absolute flow of components with an accuracy of 0.3%. The flow rate of the gas
 665 mixture can be adjusted in the range from 6 l/h to 90 l/h, but the typical value is 21 l/h, which
 666 corresponds to the exchange of 2 volumes per day. Also, one additional channel is available to

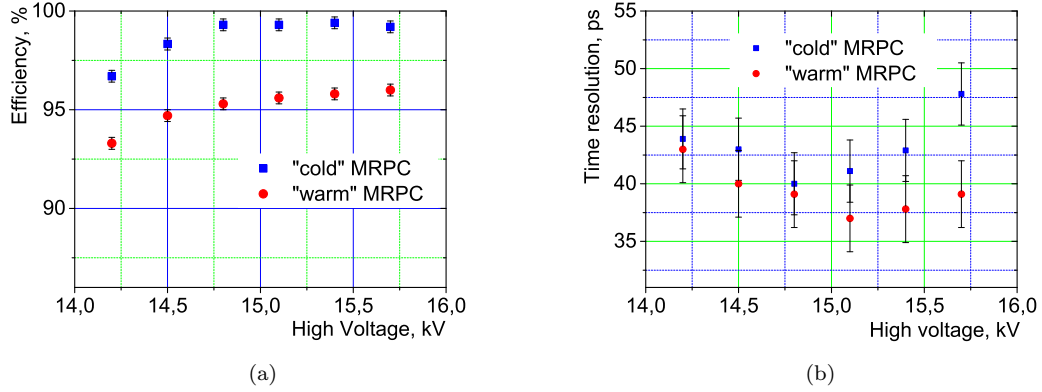


Figure 32: Performance of the MRPC designed for TOF700 system. The detectors efficiency is shown on the left and time resolution on the right.

	TOF400	TOF700
MRPC active area	30x60 cm ²	30.3x56 cm ² "cold" 16x35.1 cm ² "warm"
FEE on one MRPC	96	32 for "cold" 64 for "warm"
Number of MRPC	20	30 "cold" 40 "warm"
Total active area	2 Arms x 1.1x1.3 m ²	3.2x2.2 m ²
Total number of FEE	1920	3520

Table 5: Main parameters of TOF system.

667 purge the system with nitrogen for cleaning and drying. A special PC program has been written
 668 to control the parameters of the gas system via the Ethernet interface.

669 The MRPC detector operates at very high voltage of 12 kV and 15 kV for TOF400 and TOF700
 670 respectively. On the other hand, the dark currents of the detector are quite small at the level of
 671 tens of nA. Also, the detector is very sensitive to voltage ripples due to the large capacitive coupling
 672 between the high-voltage layer and the readout strips. Therefore, the high-voltage system is subject
 673 to high requirements for voltage stability and current measurement accuracy. The high-voltage
 674 power supply systems for both TOF sub-systems are based on commercially available ISeg modules
 675 and a specially designed HVSys power supply. Remote control of all elements of the system is
 676 organized via Ethernet interface.

677 To monitor stability of operation of the TOF sub-systems, controlled parameters are sent to
 678 the Slow Control System. The data are displayed on the website of the experiment via Grafana.
 679 The operator can see the value of the applied high voltage and measured current in the detectors,
 680 the thresholds of the amplifiers, the gas flow and the weight of the gas in cylinders, and some
 681 other parameters. In case of a malfunction, the operator receives a warning message that allows to
 682 respond in time. All monitored parameters are stored in a database and can be used in the offline
 683 analysis.

684 **8 Outer tracker**

685 The purpose of the outer tracker is to provide link between tracks measured in the central tracker
 686 and hits in the ToF-400 and ToF-700 detectors. In the **Run 8** outer tracker consisted of two large
 687 aperture drift chambers (DCH), four CSC (cathode strip chamber) with the size of the active area
 688 of $1129 \times 1065 \text{ mm}^2$ and one plane of $2190 \times 1453 \text{ mm}^2$ CSC (see Fig. 1).

689 **8.1 DCH** 

690 The drift chambers [16] have an octagonal shape with a transverse width of 2.9 m. (Fig. 33).

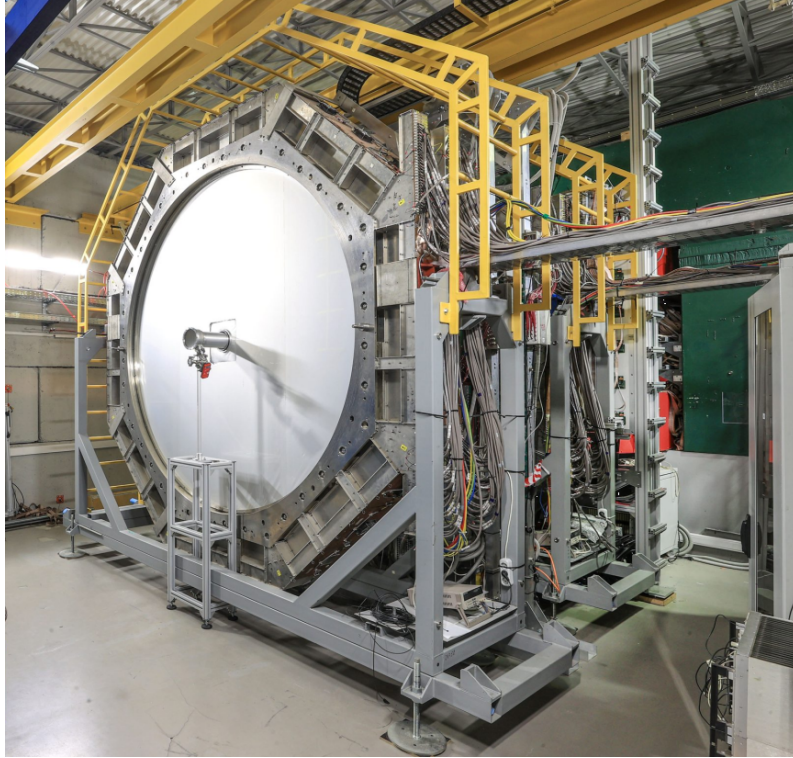


Figure 33: DCH integrated into BM@N experimental setup.

691 Their fiducial area is about 4.5 m^2 . Every drift chamber (DCH) consists of 4 double coordinate
 692 planes with the following parameters: the wire inclination angles of 0° , 90° , $\pm 45^\circ$, the wire pitch
 693 of 10 mm, the outer dimensions of the sensitive area of $Y_{\text{out}} \pm 1.2 \text{ m}$, $X_{\text{out}} \pm 1.2 \text{ m}$, the beam
 694 hole radius of $R = 160 \text{ mm}$, 256 wires per coordinate plane, 2048 wires per chamber.

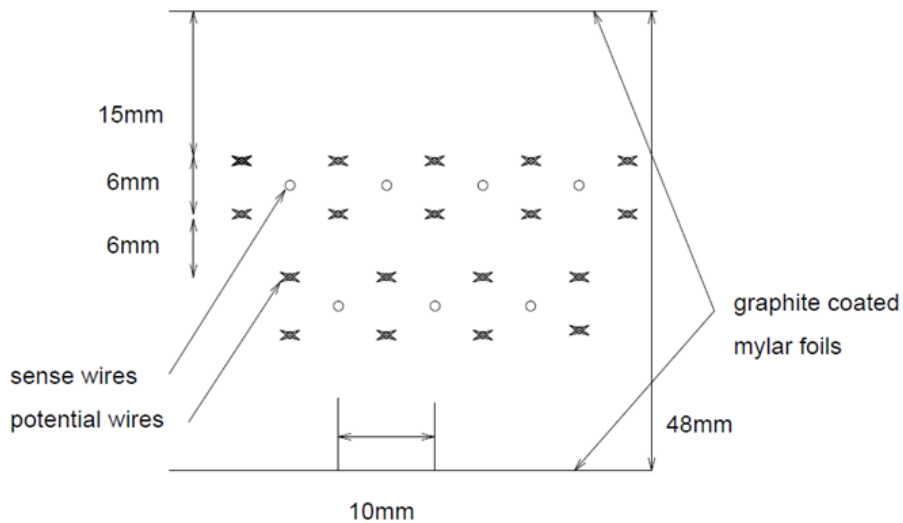


Figure 34: Drift cell geometry of the DCH.

695 To minimize multiple scattering effects, the wire chambers are constructed with minimal amount
696 of material along the beam direction. A schematic view of the geometry of one view is shown in
697 Fig.34. Sense wires have a diameter of 20 μm and made of gold-plated tungsten. The electric field
698 is created by applying a negative voltage on two planes of gold-plated Ti-Cu wires located on each
699 side of the sense wire planes, at a distance of 3 mm. The field wires have a diameter of 120 μm .
700 The spacing between sense and field wires on a plane is 10 mm. Thin Mylar foils (22 μm) coated
701 with graphite are used to shape the electric field in the drift cell and also to act as separating walls
702 between two consecutive views.

703 A readout time measurement accuracy of about 1 ns with no deadtime is achievable with
704 specially designed amplifiers and TDC circuits [17]. The anode signals in the wire chambers
705 are amplified, discriminated and transformed to logic pulses in electronic circuits located on the
706 chambers. The output pulse is a logic 50 ns wide ECL pulse with 50 ns deadtime following the
707 pulse, achieved by a delay element.

708 The granularity of DCH is sufficient to perform measurements of interactions with light ions
709 (up to Ar). The DCH wire occupancy in interactions of middle and heavy nuclei is too high to
710 perform efficient track separation. Thus, the DCH will be replaced by cathode strip chambers
711 (CSC) to perform track measurements in middle and heavy nucleus collisions.

712 8.2 CSC

713 The full configuration of the outer tracking system for heavy ion program will consist of four
714 planes of 1129 \times 1065 mm² CSC (cathode strip chamber) and two planes of 2190 \times 1453 mm² CSC.
715 The CSC detectors are situated outside the magnetic field with the aim to make precise link to
716 the tracks, reconstructed in the GEM detectors inside the analyzing magnet. Tracks refined in
717 CSC are used to improve particles momentum reconstruction and to find corresponding hits in the
718 time-of-flight systems ToF400 and ToF700.

719 The first CSC detector with the size of the active area of 1129 \times 1065 mm² was designed and
720 assembled at LHEP JINR in 2018. It consists of an anode plane located between two cathode
721 planes (see Fig. 35). The anode plane is a set of gilded tungsten wires with the diameter of 30
722 μm which are fixed on the plane with a step of 2.5 mm. The gap between the anode plane and
723 each cathode plane is 3.8 mm. Two-coordinate readout of the signal is performed on two cathode
724 PCB boards using sets of parallel metal strips. The inclination angles of the cathode strips to the
725 vertical axis are 0 degrees (X coordinate) and 15 degrees (Y coordinate). The pitch of the X and
726 Y strips is 2.5 mm. PCBs are glued to the support honeycomb. Due to a large multiplicity of
727 charged particle Au-Au collisions, readout layer is divided into outer (cold) and inner (hot)
728 zones.

729 First beam tests of the 1129 \times 1065 mm² CSC were performed in 2018 at the argon beam
730 with kinetic energy of 3.2 AGeV and the krypton beam with kinetic energy of 2.3 AGeV at the
731 Nuclotron. The CSC was installed upstream the ToF-400 time-of-flight detectors. The main goal
732 of the tests was to study the performance of the CSC detector and the FEE and readout electronics
733 as a part of the BM@N experimental setup. The signal clusters were reconstructed as groups of
734 adjacent strips with amplitudes of signals above the threshold. For the reconstructed clusters, the
735 center of gravity, the width and the total charge were calculated. The average cluster width is 6
736 strips which is equal to 15 mm. The gap size between the anode and cathode is reduced to 3 mm
737 instead of 3.8 mm in order to improve the spatial resolution in multitrack events.

738 All four CSC detectors with the size of the active area of 1129 \times 1065 mm² and one detector
739 CSC with the size of 2190 \times 1453 mm² were integrated into the BM@N setup in the physical run
740 2022-2023 with the Xenon beam at the kinetic energy of 3.8 AGeV at the Nuclotron

741 Two CSCs of the size 2190 \times 1453 mm² have been designed to cover the ToF-700 system on both
742 sides and replace the existing drift chambers (DCH). The design of these cathode strip chambers
743 is shown in Fig. 36. One cathode plane consists of 8 PCBs, each PCB is divided into hot and cold
744 zones. The hole in the center of the chamber is designed for the vacuum beam pipe. The gap size
745 between the anode and cathodes is planned to be 3 mm. Two-coordinate readout of the signal
746 is performed using sets of parallel metal strips with the inclination angle of 0 degrees for the X
747 coordinate and 15 degrees for the Y coordinate. The pitch of the X and Y strips is 2.5 mm.

748 8.2.1 Front-end electronics

749 Front-end electronics is based on the same charge sensitive pre-amplifier chip VA163 as used for the
750 GEM detectors. The multiplexed data from each board are transmitted through the twisted pair

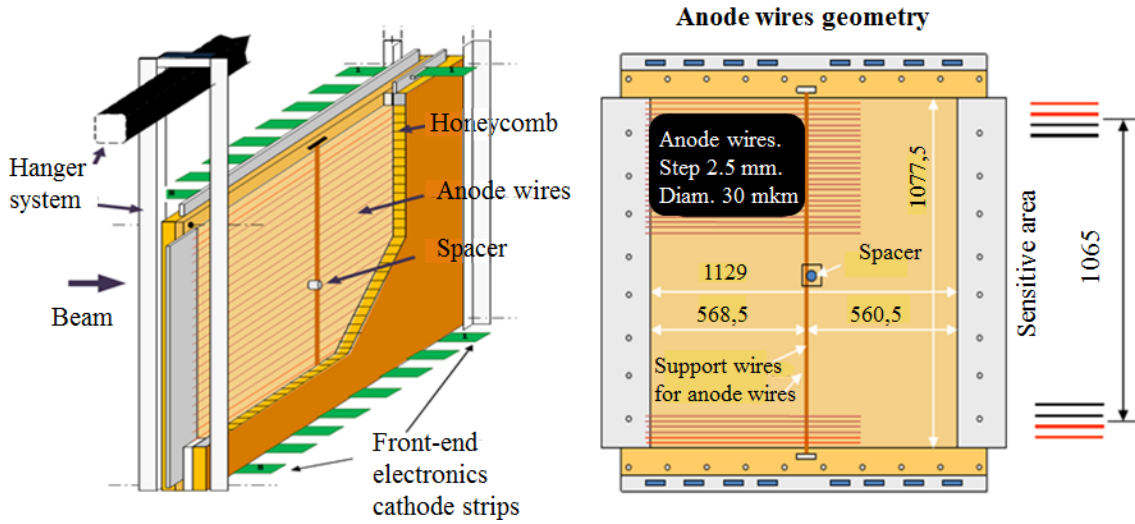


Figure 35: Schematic view of the $1129 \times 1065 \text{ mm}^2$ CSC

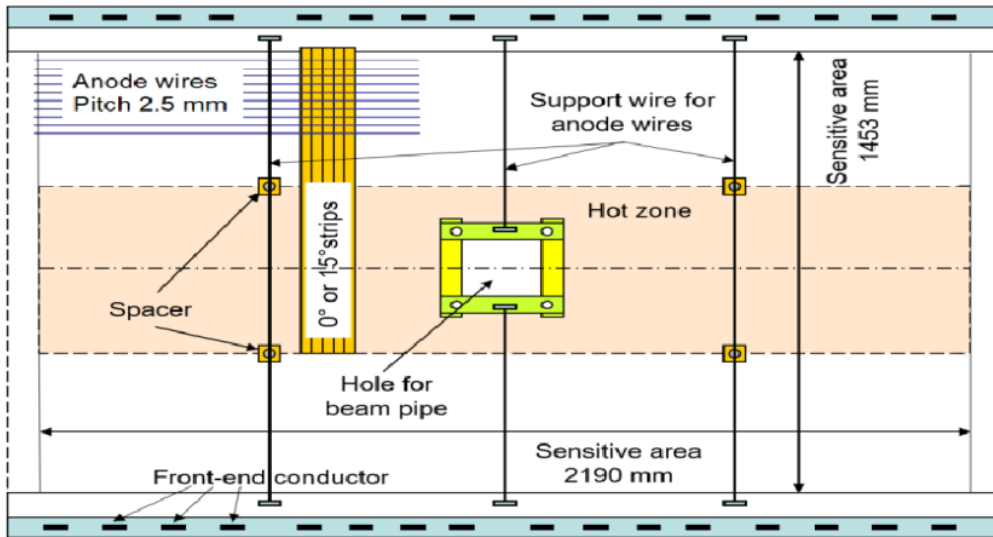


Figure 36: A technical drawing of the cathode strip chamber of the size $2190 \times 1453 \text{ mm}^2$ (15-degree strips are not shown in this picture).

751 flat cable to the 12-bit analog-to-digital converter (ADC) readout by the BM@N data acquisition
 752 system.

753 The full configuration with 6 CSC detectors equipped with the electronics based on VA-163
 754 chips (35000 readout channels) is planned to be integrated into the BM@N experimental setup at
 755 the 2023.

756 8.2.2 Gas distribution system

757 The outer tracker were operated with $\text{Ar}(75\%) + \text{C}_4\text{H}_{10}(25\%) / \text{C}_3\text{H}_8\text{O}$ (vapor) gas mixtures.
 758 The gas system (Fig. 37) consists of two parts: 1) the mixer system which delivers a mixture of
 759 gases in a required ratio and pressure to downstream elements; 2) the distribution system, which
 760 delivers the gas in well defined quantities to the individual detectors.

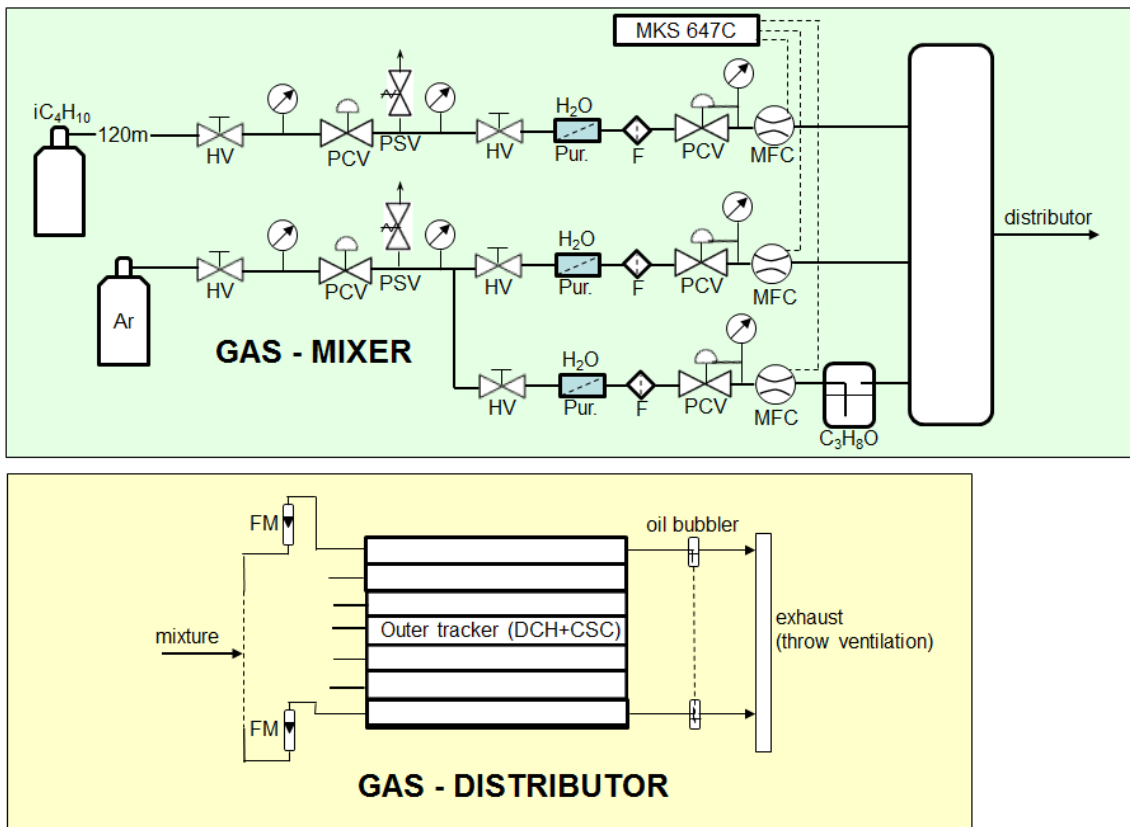


Figure 37: The gas line for the outer tracker. The layout of the mixer module: HV – on/off valve, PCV – pressure control (constant) valve, PSV – pressure safety valve, Pur. – Purifier (H₂O and O₂), F – filter, MFC – mass flow controller (MKS Instruments firm), MKS 647C – power supply and readout (MKS Instruments firm). Component layout of the distributor module: FM – flowmeter (manually flow adjustment), oil bubbler – pressure and air protection.

9 Forward Spectator Detectors

The new forward detectors for measuring the energy (FHCAL) and charges (FQH, ScWall) of projectile spectators produced in the nucleus-nucleus collisions in the BM@N experiments have been developed and constructed during last few years. They are located at the very end of the BM@N facility. These detectors are used to determine the centrality and orientation of the reaction plane. Moreover, ScWall and FQH can be used also to study the charge distributions of spectator fragments produced in the nucleus-nucleus interactions.

9.1 Forward Hadron Calorimeter (FHCAL)

The forward hadron calorimeter FHCAL has a granular structure in the transverse and longitudinal planes. It consists of 54 separate modules which provides transverse granularity of the FHCAL. Internal part of the FHCAL consists of 34 small modules with transverse sizes of $15 \times 15 \text{ cm}^2$ and a length equivalent to 4.0 nuclear interaction lengths. These modules are identical to the modules of the forward hadron calorimeters of the Multi-Purpose Detector (MPD) experiment at the NICA accelerator complex [8]. Two outer lateral parts of the calorimeter consist of 10 large modules on each side with transverse sizes of $20 \times 20 \text{ cm}^2$ and a length equivalent to 5.6 nuclear interaction lengths. These modules were initially constructed for the hadron calorimeter of the Compressed Baryonic Matter (CBM) experiment (FAIR, Darmstadt, Germany) [9] and are temporarily used in the hadron calorimeter of the BM@N experiment. Schematic view of the FHCAL is shown in Fig. 38, left. At the center of the calorimeter there is a hole with transverse size $15 \times 15 \text{ cm}^2$. Noninteracted beam ions pass to a beam dump located behind the calorimeter through this hole. It is necessary to protect internal modules of the calorimeter against high radiation dose and strong activation in experiments with heavy ion beams.

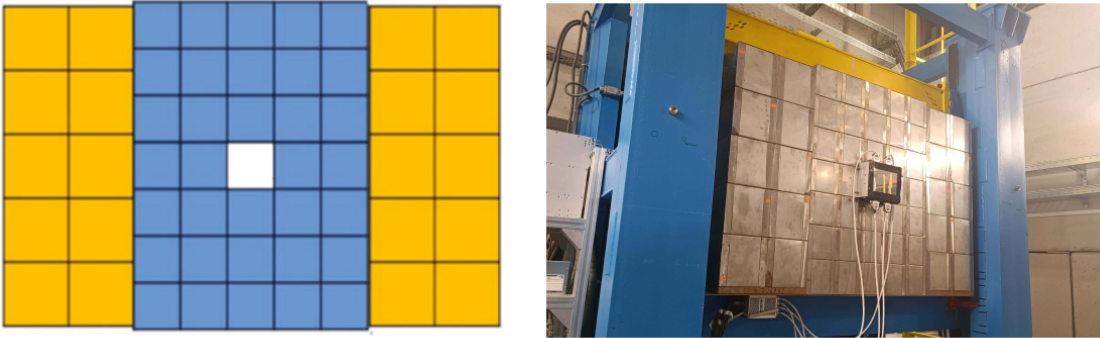


Figure 38: Schematic view of the FHCAL, left. Photo of the FHCAL with FQH installed on the the movable platform (blue) at the BM@N, right.

FHCAL modules have sampling structure and consist of lead/scintillator layers with a sampling ratio of 4:1 (the thickness of the lead plates and scintillator tiles are 16 mm and 4 mm, respectively) and provide compensation condition ($e/h=1$) for the hadron calorimeter. Small modules have 42 lead/scintillator layers and large modules have 60 such layers. To get rather hard rigidity of the lead plates they are made of lead-antimony alloy. An assembly of 60 (42) alternating layers of scintillator and lead plates are tightened into one package with a 0.5 mm thick stainless steel band using a special tensioning mechanism. The tape is welded with spot welding to the steel plates inserts installed in the beginning, middle and end of the package (Fig. 39). Behind the tightening mechanism the block of boron polystyrene with thickness 10 cm is installed in large modules. Once the package is assembled, it is closed by an upper box of 0.5 mm thick stainless steel sheet.

The scintillator plates are made from polystyrene-based plastic scintillators produced by Uniplast (Vladimir, Russia). Light from each scintillator plate is collected by wavelength shifting optical fiber KURARAY Y-11(200) glued into groove with depth 1.2 mm on the surface of the scintillation plate and transported to the end of module. The grooves in scintillators of large modules have circular form, while grooves in scintillators in small modules are spiral. Outside of the scintillator plate fibers are placed in thin black plastic pipes to be optically shielded and are stacked in parallel on the top surface of the module package. All scintillators with glued fibers are wrapped in Tyvek reflector.

801 The end of each fiber glued in the scintillator plate is coated with reflective paint. At the
 802 end of the module the optical fibers from each of the six consecutive scintillation plates in the
 803 module are glued into individual optical connectors, which are placed on a panel mounted in the
 804 module box. Thus, each of large modules has ten longitudinal sections and each of small modules
 805 has seven sections. The longitudinal segmentation provides high homogeneity of light collection
 806 along modules, a large dynamic range of the calorimeter response and makes it possible to perform
 807 energy calibration of FHCAL with cosmic muons [10].

808 This panel with ten optical connectors for large module (seven optical connectors for small
 809 module) has an additional optical connector for LED light distribution system. LED pulses are
 810 distributed with ten (seven) optical fibers into each section optical connector. Light pulses from
 811 the LED allow to control the operation of the photodetectors used for light readout.

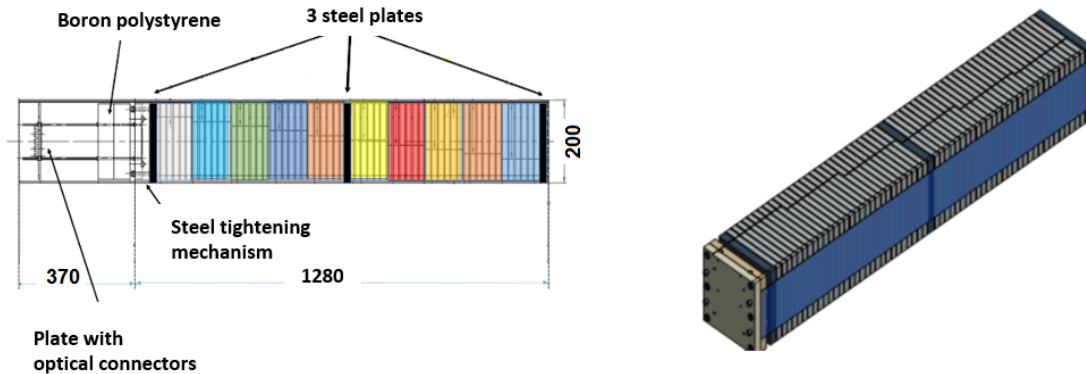


Figure 39: Left - scheme of large module, here 10 sections are shown in different colors. Right - 3D view of the large calorimeter module in assembly.

812 The weight of each small module is about 200 kg and weight of large module is about 500 kg.
 813 Total weight of the FHCAL is about 17 tons. It is mounted on the special platform shown in blue
 814 color on Fig. 38, right, which is able to move FHCAL in X-Y directions.

815 9.1.1 FHCAL photodetectors, FEE and readout electronics

816 The Hamamatsu MPPC S12572-010P with $3 \times 3 \text{mm}^2$ sensitive area are used as photodetectors for
 817 light detection from the sections of the FHCAL. These photodetectors have gain 1.35×10^5 and
 818 photon detection efficiency about 10% at peak sensitivity wavelength 470 nm. Due to very small
 819 pixel pitch - 10 μm - the total number of pixels is 90000 which is important to provide the linear
 820 response in wide dynamic range of the signal. FHCAL Front-end-electronics (FEE) is composed of
 821 two separate PCBs. Ten (seven) photodetectors are installed on a first PCB directly connected
 822 with light connectors at the end of each large (small) module. A temperature sensor is mounted
 823 near photodetectors on aluminum heat sink. The second PCB contains signal preamplifiers with
 824 differential ADC driver output and individually adjustable voltage regulation circuits for the pho-
 825 todetectors. This board has also LED flash generation circuit with synchronization input and
 826 analog sum signal output. All FEE boards are remotely controlled via specially designed HVSys
 827 System Module manufactured in JINR (Dubna, Russia).

828 There are 438 calorimeter sections, which are needed to be readout. Eight ADC64s2 boards,
 829 produced at JINR (Dubna, Russia) are used for signal readout. They have 64 channel 12-bit
 830 ADCs with sampling rate of 62.5 MHz and memory depth of up to 1024 points per channel.
 831 The ADC64s2 boards have Lemo connectors for trigger and Xoff signals, and are capable of time
 832 synchronization via White Rabbit network, providing per-channel zero suppression function with
 833 adjustable threshold and can operate in self-triggered or externally triggered modes. FHCAL ADCs
 834 are fully integrated into the BM@N data acquisition system which provides trigger signals, busy
 835 logic, White Rabbit network and data readout. Power for FHCAL ADCs is provided by a remotely
 836 controlled power supply units placed in Wiener crate.

837 Custom 12-channel analog sum modules (adders) with individually adjustable attenuation have
 838 been constructed. These adders are used to sum up the analog outputs from FHCAL modules. They
 839 are used when performing standalone cosmic calibrations in central DAQ. The adders can be used
 840 for integration into the BM@N trigger system.

841 **9.1.2 FHCAL calibration with cosmic muons, energy resolution and linearity of the**
 842 **response**

843 Since muon beams are unavailable at the BM@N setup, energy calibration of the FHCAL can only
 844 be performed using cosmic particles. Longitudinal and transverse segmentation of the calorimeter
 845 allows for track reconstruction [10], which was used to compensate for track length variation in
 846 the scintillator tiles due to varying track orientation of the cosmic particles. Cosmic calibrations
 847 parameters show 40 - 50 photoelectrons per one muon per one section.

848 A detailed study of the linearity of response and energy resolution for array of 9 large modules
 849 has been performed on protons with kinetic energy range 1 - 9 GeV at the CERN T9 and T10
 850 beamlines [11]. The good linearity and $0.54/\sqrt{E}$ energy resolution was obtained.

851 **9.2 Forward Quartz Hodoscope (FQH)**

852 The FHCAL beam hole is covered with beam hodoscope - Forward Quartz Hodoscope (FQH). The
 853 main goal of the FQH is measuring charges of spectator fragments which pass the beam hole of
 854 the calorimeter in order to estimate the collision centrality with combined FHCAL and hodoscope
 855 response. The FQH consists of 16 strips - cherenkov detectors - with sizes of $16 \times 1 \times 0.4\text{cm}^3$
 856 (see Fig. 40, left) inside light tight box. Each FQH detector has light readout with two individual
 857 silicon photo-multipliers mounted on opposite sides of the strip (see Fig. 40, right).

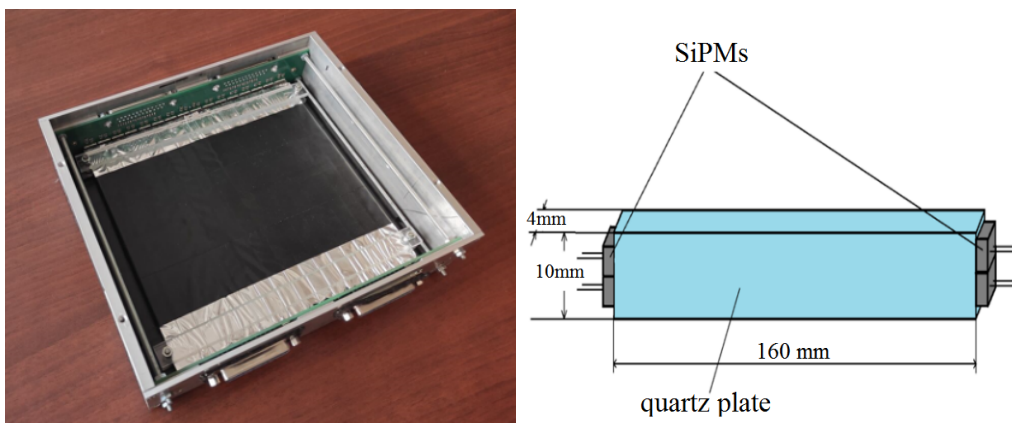


Figure 40: Left: photo of Forward Quartz Hodoscope - FQH (inside view). Right: picture of the FQH strip with SiPM photodetectors mounted.

858 One Front-End-Electronic (FEE) board reads eight channels. Total number of FEEs are four
 859 for full FQH. The FQH installed in front of the beam hole of FHCAL is shown in Fig. 38 (right).
 860 Four FEE boards of FQH are connected to the control box with amplifiers installed at bottom side
 861 of FHCAL.

862 Hamamatsu MPPCs S14160-3015PS with $3 \times 3 \text{ mm}^2$ sensitive area and PDE of 32% are used
 863 as photodetectors. Four TQDC-16 boards with total 64 channels are used to read-out the two-
 864 gain outputs from each photodetector. The gains are 1x and 4x. Low gain channel is used for
 865 maximum dynamic range up to the highest ion charge expected. High gain channel is used for
 866 low-Z fragments. Charge calibration of FQH strips is performed with pure beam ions.

867 **9.3 Scintillation Wall (ScWall)**

868 The ScWall is the large area detector aimed for measuring the charged particles in forward rapidity.
 869 It consists of array of scintillating plates placed in the aluminum box. The view of the ScWall
 870 is shown in Fig. 41. The full detector size is $270 \times 130\text{cm}^2$. The ScWall has 40 inner small
 871 ($7.5 \times 7.5 \times 1\text{cm}^3$) scintillator detectors (cells) and 138 big outer cells ($15 \times 15 \times 1\text{cm}^3$). In order to
 872 avoid heavy-ion beam radiation damage the very central part of ScWall has $15 \times 15\text{cm}^2$ beam hole
 873 (see Fig. 41). The cells are made of polystyrol-based scintillators are manufactured at “Uniplast”
 874 (Vladimir, Russia).

875 The light in the cells is collected by WLS Y11(200) S-type (Kuraray) fibers mounted in 1.5mm
 876 deep grooves (see Fig. 42) and detected by SiPM Hamamatsu S13360-1325CS with $1.3 \times 1.3\text{mm}^2$
 877 active area, gain of 7×10^5 and PDE of 25%. The measured light yields of big cells and small cells
 878 are about 32 p.e./MIP and about 55 p.e./MIP, respectively. The full area of ScWall is divided
 879 into 12 read-out zones and performed with ADC64s2 board combined with FEE boards. Three

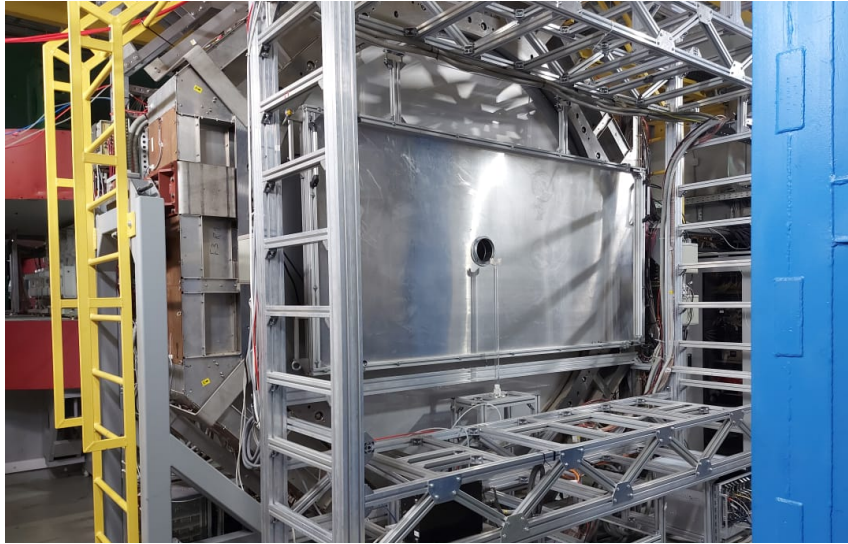


Figure 41: The view of ScWall detector with the beam hole.

880 ADC64s2+FEE boxes are used for read full ScWall. The calibration of ScWall cells has been
 881 performed on cosmic muons as well as on Z=1 charge particles coming from the ion-ion reaction.

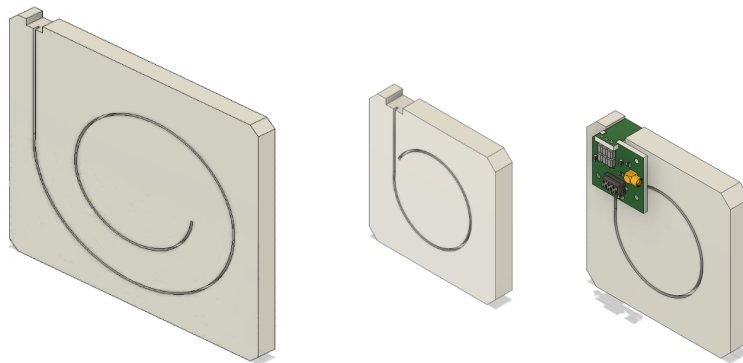


Figure 42: From the left to the right: schematic view of large ScWall cell, schematic view of small ScWall cell, schematic view of small cell assembly with SiPM on PCB board with connectors.

882 9.4 Slow Control for forward detectors

883 The FHCAL, FQH and ScWall have SiPMs as light detectors. In order to control and monitor
 884 bias voltage (HV) applied to SiPMs and the temperature the new Slow Control system has been
 885 developed. The hardware part of Slow Control is designed and constructed by “HVsys” (JINR,
 886 Dubna). HV power supply modules have multi-channel HV supplies with micro-controller interface.
 887 Schematic view of Slow Control system is shown in Fig. 43. Each HVsys system module has a
 888 unique IP-address for communication through individual proxy-server. Communication of HVsys
 889 box with FEE micro-controllers is done with RS-485 interface. All proxy-servers have connections
 890 to GUI panel to control and monitor status and to perform temperature correction for all SiPMs.
 891 The software part of the Slow Control is written on python3 [12].

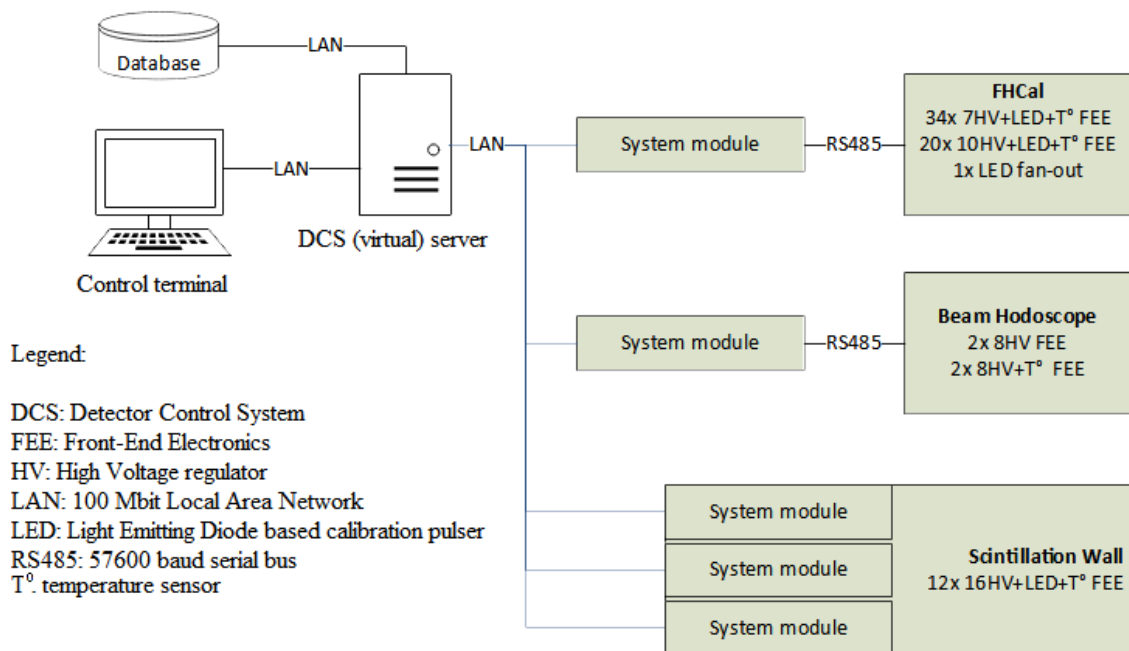


Figure 43: The Slow Control system for forward detectors at BM@N.

10 Trigger

BM@N trigger consists of hardware and software parts. The hardware part includes detectors on fast plastic scintillators, low- and high- voltage power suppliers, programmable trigger logic unit T0U, trigger control unit CAEN N6742. The software part include a graphic trigger interface, trigger performance and beam quality control.

A beam trigger BT formed by the signal coincidence from beam counters BC1, BC2 under condition the signal absence from the veto counter VC:

$$BT = BC1 \times BC2 \times VC(veto)$$

A minimum bias trigger MBT asks only for a low amplitude signals in forward counter FD, which corresponds to the beam particle interaction in a space between BC2 and FD counters:

$$MBT = BT \times FD(veto)$$

The interaction trigger called Central Collision Trigger (CCT) composed of the minimum bias trigger and the multiplicity in the barrel detector:

$$CCT = MBT \times BD(> N)$$

All the triggers mentioned above (BT, MBT, CCT) are send in the output data stream with the corresponding scaling factor.

Trigger decision formed by the programmable logic controller T0U and its logic organisation is shown in Fig. 44.

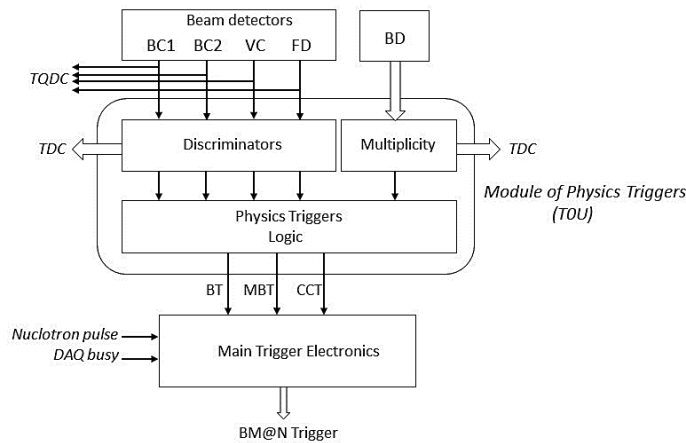


Figure 44: Trigger logic.

11 BM@N DAQ: Hardware Architecture

The core function of the DAQ system is realization of data transfer from the detector to the storage system. It includes the data flow from readout electronics to the First Level Processor (FLP) fabric, to the Event Building (EB) and to the Storage System. Main DAQ components are readout electronics modules, clock and time synchronization system, trigger distribution system, data transfer networks, data processing service and online storage system (*link - to - tdr*). The general architecture is sketched in Fig. 45.

Detector Readout Electronics (DRE) boards record detector signals. There are two main types of DRE boards grouped by function: Timestamping Time to Digital Converters (TDC), Waveform Digitizers or Amplitude to Digital Converters (ADC).

11.1 TDC DRE board

TDC DRE board performs time-stamping of discrete signals (hits) with typical accuracy of $20ps$. It is based on HPTDC chip. Hit timestamps are kept for $51\mu s$ in ring type memory. The total trigger latency should not exceed this value. ADC DRE board is a waveform digitizer. It quantize analogue input signal and samples it at fixed time intervals. Zero suppression logic is based on baseline estimation and threshold value. Signal shaping can be performed in digital form with FIR filters. It allows to reduce the number of waveform points required for digital signal representation with minimum loss of accuracy. The ring type memory allows the read back of last $32\mu s$ of waveforms. It sets the limit on trigger latency to this value. TQDC DRE board combines both TDC and ADC functions.

11.2 MSC16VE module

MSC16VE is 16-channel multievent scaler (Fig. 47). Each channel input has 50Ω impedance and accept signals of $\pm 2.5V$ range and discrimination threshold can be adjusted in $\pm 1V$ range. Module has 4 LVTTTL count enable (CE) inputs. Ethernet 1000BASE-X connection is used for data readout and module control. Module MSC16VE has three main logic parts: input part, multi-event data readout and hardware histograms. Input part has crosspoint switch that allows any input channel to be processed by any multi-event counter and histogram. CE and Gate logics have 16 independent Look-Up Tables (LUT) each. Gate logic determines reset conditions for hardware histograms. Multi-event counters data continuously splits into numbered time slices and pushes to data encoder and further to Ethernet. Time slices length is adjustable with minimum length of $64 ns$ and $8 ns$ step. Data encoder perform zero suppression and data packing. Hardware histograms are used for online monitoring of input hits. Time series histograms store hits distribution in time. Time interval histograms store time interval between two adjacent hits in channel. Both hardware histograms readout by request from control software.

11.3 Timing System

White Rabbit provides sub-nanosecond accuracy and picosecond precision of time synchronization for distributed systems. DRE boards digitize detector signals using common notion of time and frequency provided by the White Rabbit (WR) network. The time reference is provided by GPS/GLONASS receiver and backup precision frequency reference (Rubidium clock). Digitizer boards require precise reference clock for high precision measurements. Timestamping TDCs used in T0, TOF400, TOF700 detector electronics have time resolution of $25ps$, DCH-100ps. DRE boards include White Rabbit Node Core and tunable crystal oscillators that are synchronized to reference clock with $10ps$ accuracy. WR node core provides local clock and timestamp at 125 MHz. The timestamp is specified as TAI (International Atomic Time). It is an absolute number of seconds and nanoseconds since 01.01.1970. Frequency dividers synchronized by 1 PPS (Pulse per Second) signal are used to produce digitizer clocks: 41.667 MHz for HPTDC ASICs and 62.5 MHz for waveform digitizers.

11.4 Trigger distribution system

BM@N trigger system has tree structure and 3 trigger levels: L0, L1 and L2.

956 **11.4.1 General architecture of trigger distribution system**

957 L0 is fast trigger signal for front-end electronics with latency of $150ns$. L1 trigger signal is readout
 958 trigger candidate generated by TRC module (see 11.4.2), according to its internal logic. Formation
 959 time of L1 trigger is adjustable and was $1\mu s$ in BM@N run 8. L2 trigger, produced by UT24VE
 960 module (see 11.4.3), starts data readout for all subsystems. All signals are transmitted via coaxial
 961 cables in LVTTTL standard. Trigger-Busy handshake algorithm for L2 trigger was implemented to
 962 guaranty all triggers delivery to all subsystem. This algorithm is shown in the Fig. 48. Rising edge
 963 of trigger signal (1) leads to rising edge of busy signal (2). After that trigger signal is deasserted (3).
 964 Upon completion of data collection, the subsystems deassert busy signals (4). Typical subsystems
 965 busy time shown in the Fig. 49.

966 **11.4.2 TRC – Trigger Control**

967 TRC (TRigger Control) module was designed for BM@N run 8. Main goal of this module is
 968 production of readout trigger candidates (L1) according to its configurable logic. T0 unit is used
 969 as source for input signals (“physical” triggers BT, CCT, MBT, etc.). Each of 16 input channels has
 970 individual settings: input delay, hits downscaling factor and before/after protection. Before/after
 971 protection logic used for pile-up rejection and secondary hits rejection during detectors dead time.
 972 L1 trigger candidate output delay can be adjusted in range of $8 ns$ to $100 \mu s$. TRC module produces
 973 L0 trigger for GEM, CSC, FSD and BT front end electronics, as they required fast (less than 300
 974 ns) data latch signal. Different conditional counters for input physical triggers are implemented
 975 in TRC module.

976 **11.4.3 LTU - Logical Trigger Unit**

977 LTU is main module for L2 trigger generation and distribution system. The module ensures the
 978 operation of Trigger-Busy handshake algorithm (Fig. 48) and can process up to 16 busy channels.
 979 Busy signals can be received from DRE modules or hierarchically lower LTU modules. Time
 980 intervals between accepted triggers and busy signals duration are histogrammed in LTU internal
 981 memory. Various trigger counters are also implemented in module.

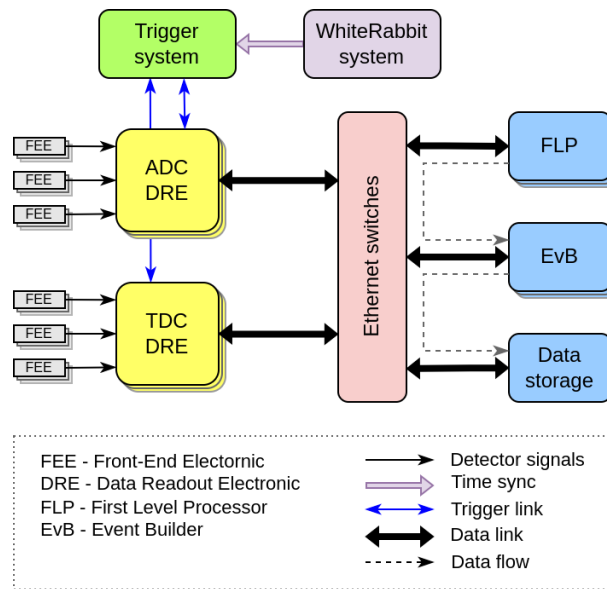


Figure 45: General architecture of DAQ system

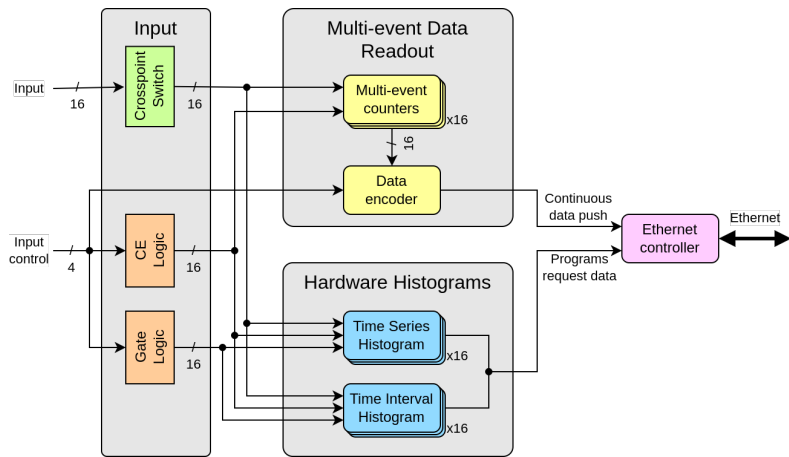


Figure 46: MSC16VE module.

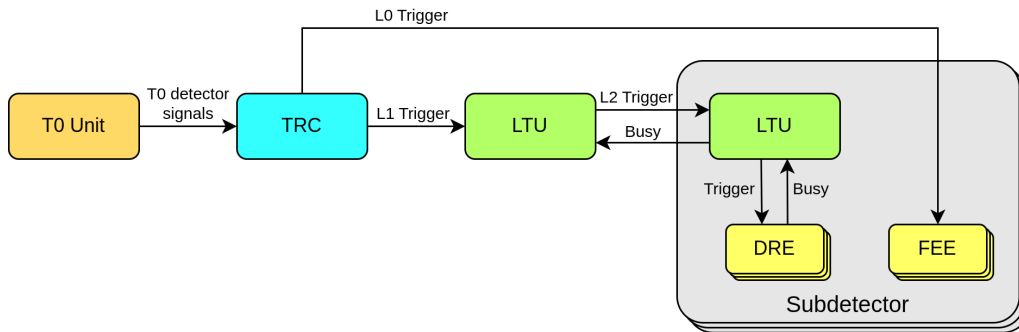


Figure 47: BM@N trigger architecture.

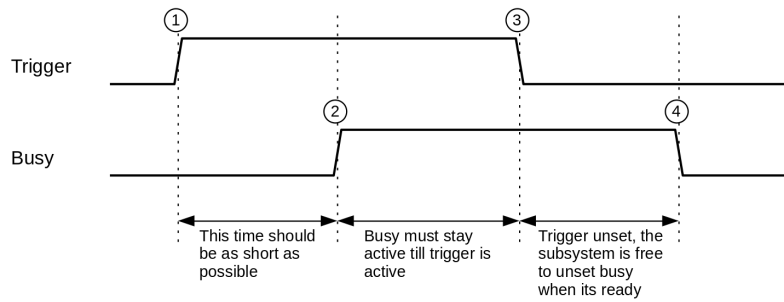


Figure 48: Trigger handshake chronogram.

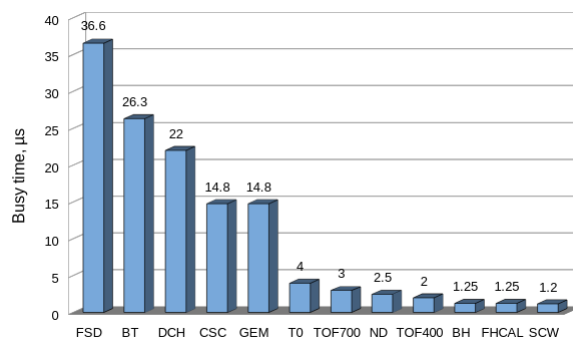


Figure 49: The average busy time for all subsystems.

11.5 DAQ data flow

All BM@N subdetectors except DCH use Ethernet to transfer data from readout electronics to First Level Processors. Primary FLP task is to receive data stream in real time, buffer, validate, format and enqueue data blocks to event building network. FLP decouples fast microsecond-scale synchronous data acquisition process from slower seconds-scale software data processing by buffering data in computer RAM. Data transfer path from readout electronic module to event building network and storage system is shown on Fig. 50 for typical 64-channel ADC based waveform digitizer module ADC64VE.

Electronic modules designed by DAQ team share common communication architecture. Network connectivity is provided by hardware IP stack (HWIP), a programmable logic code synthesized for onboard FPGA processor. Taking into account limited memory and logic resources of FPGA chips available, and implementation complexity of TCP protocol, custom data transfer protocol MStream has been designed for data streaming over 1 Gb/s or 10 Gb/s Ethernet networks. It uses UDP over IP as transport layer, and implements ordered and reliable data packet delivery using acknowledgments.

FLP receive data stream in real time. Dedicated servers with dual 18-core CPUs, equipped with dual 100 Gb/s Ethernet adaptors, are running Fedora-36 Linux OS. Tuning for real-time operation is necessary to ensure continuous data transferred without interruptions [18]. It includes CPU frequency and supply voltage management, network adapter interrupt coalescence mitigation and system task scheduler adjustments.

BM@N readout electronics deliver 6 GB/s of raw data over 200 streams in peak at 10 kHz trigger rate. Single data stream has 500 MB/s maximum sustained throughput when using 10 Gb/s Ethernet. Run 8 operation has shown that single manually tuned FLP server is capable of hosting 10-12 data stream receivers with minimal contribution to overall busy time.

Software event building in BM@N is part of asynchronous processing, it does not affect readout busy time under normal operation. Event builders are cascaded in multiple layers for load distribution, and last layer writes data files to storage system.

Event Builder programs associated with data intensive subdetectors run on dedicated hardware servers, while event builders for low data rate subdetectors run in KVM virtual environment, as well as readout control programs. It allows to utilise computer resources efficiently.

11.6 DAQ storage system

DAQ storage system is comprised of 10 servers with NVMe solid state devices for low latency I/O operations and 12 servers with hard disks for high volume storage. It is distributed software defined object storage cluster under control of Ceph software ([19]). Cluster management and interface functions are implemented on 6 dedicated single-CPU servers. Configurable ‘CRUSH map’ algorithm defines data object to storage device mapping. Ceph cluster has self recovery functions and it performs periodic data read check on regular intervals to ensure data integrity. It is highly available and reliable system with no single point of failure.

Storage devices are organised in pools with different data redundancy algorithms. Pools allocated on NVMe devices have triple replication provide 100 TB usable space, and are used as block storage for virtual machine cluster. Hard disk pool has 2.2 PB usable capacity. It use erasure coding replication with 40% overhead. POSIX compatible filesystem interface CephFS is used for experimental data storage. Server hardware characteristics are shown in Table 6.

Qty	Function	Specifications	Network
20	Compute node	Dual 18-core 3 GHz CPU, 384 GB RAM	Dual 100 Gb/s
10	NVMe storage server	10 × 3.5TB NVMe	Dual 100 Gb/s
8	HDD storage server 1	24 × 12TB HDD, 1.8TB SSD cache	Dual 100 Gb/s
4	HDD storage server 2	24 × 18TB HDD, 3TB SSD cache	Dual 100 Gb/s
6	Control server	4-core CPU, 64 GB RAM	Dual 25 Gb/s
1	Bootstrap server	4-core CPU, 16 GB RAM, 4 × 300GB HDD	Dual 1 Gb/s

Table 6: Characteristics of BMN DAQ server equipment.

11.7 Virtual computing cluster

Programs performing readout control functions, detector slow control, software and infrastructure monitoring and other services are run on KVM virtual machines or LXC containers that reside on

1028 highly available cluster. Approx. 100 virtual machines in total reside on 10 compute nodes. Cluster
 1029 has backup and snapshot rollback mechanisms that are necessary for safe software administration
 1030 and recovery in case of errors. Virtual cluster is also used as offline computing farm for batch and
 1031 interactive analysis when no data taking is in progress.

1032 11.8 BM@N DAQ IT Infrastructure

1033 DAQ server equipment is located in 4 racks in MDC (modular data center), Fig. 52 49 servers
 1034 occupy 81 units of rack space in total. Table ?? shows server types and functions.

1035 Virtual machine cluster is comprised of 10 compute nodes running Proxmox VE version 7
 1036 software. Other 10 compute nodes are dedicated servers for FLP and event builders and run
 1037 Fedora-36 OS. Storage servers run CentOS 8 Stream OS.

1038 Basic network infrastructure services (RADIUS, DHCP, DNS) are provided by virtual cluster
 1039 with redundancy. During cold startup, while virtual cluster is not yet ready, basic services are
 1040 provided by bootstrap server. By design DAQ system is not dependant on any external network
 1041 or software services and autonomous operation is possible.

1042 Core of data network is two-level Ethernet fabric with Clos architecture that has two switches
 1043 on spine level and multiple switches on leaf level Fig. 51. Ethernet VPN (EVPN) virtualisation
 1044 technology is used to allow flexible traffic management, high availability and efficient link utilisation.
 1045 Underlay network provide connectivity between fabric nodes, it is formed by leaf and spine
 1046 switches connected with L3 routed links, topology is managed by OSPF dynamic routing protocol.
 1047 Overlay network that carry user traffic is realised with MP-BGP protocol at control plane and
 1048 VXLAN encapsulation at data plane.

1049 DAQ network supports jumbo ethernet frames up to 9000 bytes to maximise throughput of
 1050 data transfer from readout electronics. Network supports Any-Source Multicast that is necessary
 1051 for automatic discovery of readout electronics modules and software components of distributed
 1052 DAQ system.

1053 Two spine and four leaf switches are located in racks of MDC. Other leaf switches and access
 1054 switches of slow control systems are located in electronics racks in experimental area. Two core
 1055 routers of DAQ technological network are located in building 201 and provide connectivity to
 1056 campus network with 200 Gb/s bandwidth.

1057 Compute and storage servers, readout electronics and additional level of 1 Gb/s access switches
 1058 for slow control systems are connected to fabric leaf switches. Critical components have dual
 1059 connections to pairs of leaf switches for high availability using LACP link aggregation protocol.

1060 DAQ network has shown no critical problems during BMN data taking Run 8. Ethernet switch-
 1061 ing fabric bandwidth is adequate for peak traffic conditions and has no negative impact on data
 1062 taking performance. No significant packet drops or errors were registered by monitoring system
 1063 on network fabric switches that could indicate network saturation and packet buffer overflows.
 1064 Considering both trigger rate and event size increase on next data taking run, it is possible to
 1065 double fabric bandwidth by additional leaf to spine connections.

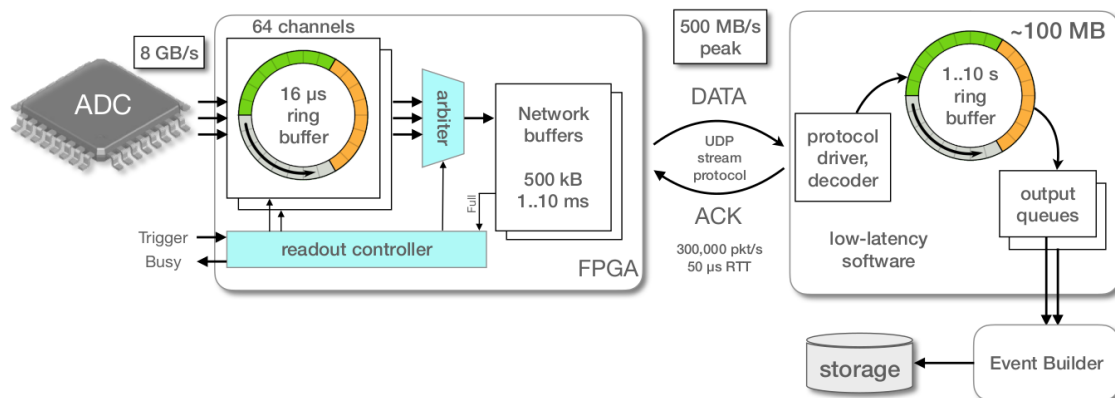


Figure 50: Data transfer from detector to storage system.

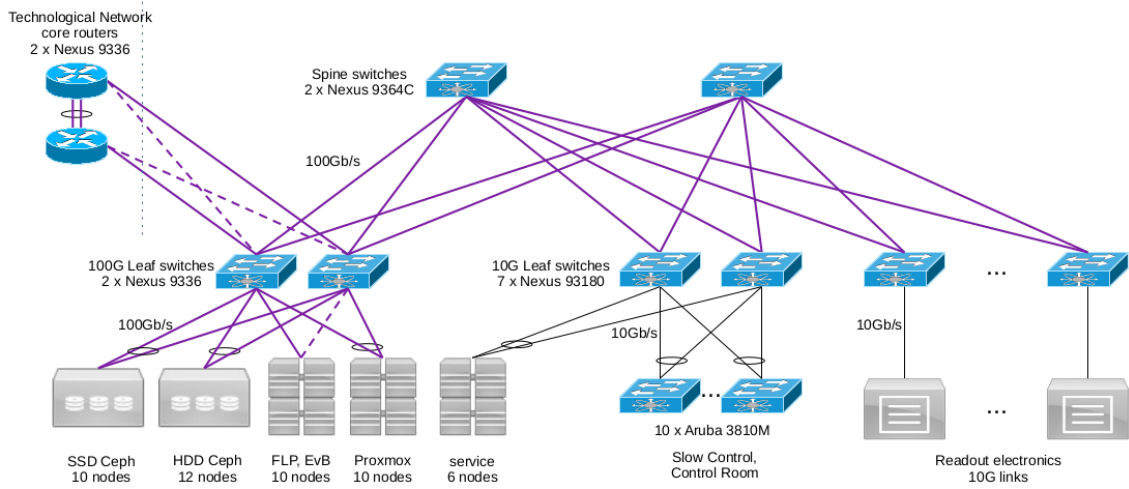


Figure 51: BMN DAQ Network.



Figure 52: BM@N Modular Data Center server racks.

1066 **12 Slow Control System**

1067 Main objectives of Slow Control System (SCS) include hardware status monitoring, archiving
 1068 the operational properties of the facility, user-friendly graphical interface and alarm management
 1069 system. The SCS was built around “TANGO Controls” [20] - an open-source toolkit, widely used
 1070 in scientific experiments.

1071 Slow Control data from experiment subdetectors such as: high voltage, low voltage, vacuum,
 1072 gas flow and mixture etc. are aggregated by SCS. Those are then stored in the “historical database”
 1073 - a PostgreSQL database with TimescaleDB extension [21]. It is implemented as distributed cluster
 1074 with backup and load balancing

1075 The user interface for live monitoring and retrieving past data is developed with Grafana [22]
 1076 – an open-source analytics and interactive visualization web application. A mnemonic scheme of
 1077 the experiment displaying hardware status and alarms (Fig. 53) was also implemented with it.

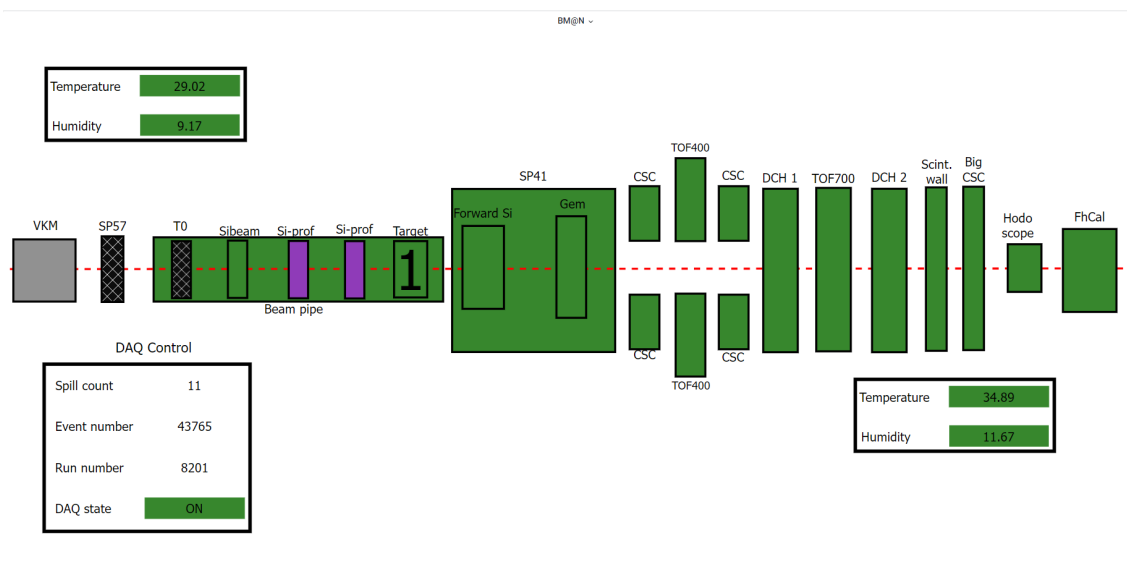


Figure 53: Slow Control System Main View.

1078 TANGO Database, hosting the configuration of the whole system, and TANGO Historical
 1079 Database are running on the BM@N virtual machine cluster. While programs, controlling and/or
 1080 monitoring real hardware are running either on virtual cluster or on dedicated PCs of different
 1081 subdetectors.

1082 **13 Summary**

1083 The detailed description of BM@N spectrometer is given. In this configuration t the fall of 2022 and
1084 the beginning of 2023 a big data set was recorded during 3 moths period. About 500M events with
1085 the different trigger condition are available for a physical analysis. A preliminary ananalysis of about
1086 1% of data shows a signals particles decays with strange quarks (K_S^0, Λ). The signature of charge
1087 pions, kaons and protons is visible if the time flight system TOF400/TOF700 is involved in the
1088 data analysis. The resolution in particle momentum, the width of the invariant mass distributions
1089 are in agreement with the expected values estimated by MC simulation. The BM@N collaboration
1090 acknowledges the efforts of the staff of the accelerator division of the Laboratory of High Energy
1091 Physics at JINR that made the data taking possible and successful. The BM@N collaboration
1092 acknowledges support

References

- 1093
- 1094 [1] M. Kapishin (for the BM@N Collaboration), Eur. Phys. J. A52 (2016) no. 8, 213.
- 1095 [2] J. Randrup and J. Cleymans, Phys. Rev. C 74 (2006) 047901.
- 1096 [3] B. Friman, W. Nörenberg, and V.D. Toneev, Eur. Phys. J. A 3 (1998).
- 1097 [4] NICA White Paper, Eur. Phys. J. A 52 (2016).
- 1098 [5] BM@N Conceptual Design Report: http://nica.jinr.ru/files/BM@N/BMN_CDR.pdf
- 1099 [6] Ch. Fuchs, Prog. Part. Nucl. Phys. 56 (2006) 1-103.
- 1100 [7] P. G. Akishin *et al.* Optimization of a Large Aperture Dipole Magnet for Baryonic Matter
- 1101 Studies at Nuclotron, Phys. Part. Nucl. Lett. 2015. V. 12. P. 305
- 1102 [8] A. Ivashkin *et al.* <http://mpd.jinr.ru/doc/mpd-tdr/> 2017
- 1103 [9] F. Guber *et al.* <http://repository.gsi.de/record/109059/files/20150720> 2015
- 1104 [10] A. Izvestnyy, N. Karpushkin, F. Guber, S. Morozov and O. Petukhov, Calibration of FHCaI
- 1105 with cosmic muons at the BM@N experiment, J. Phys. Conf. Ser. 1690 (2020) no.1, 012060.
- 1106 [11] N. Karpushkin *et al.* Study of the hadron calorimeters response for CBM and BM@N experi-
- 1107 ments at hadron beams, J. Phys. Conf. Ser., 2020. 2013-2013 Vol. 1667, no. 1. P012020. DOI:
- 1108 10.1088/17426596/1667/1/012020.
- 1109 [12] O. Petukhov, S. Morozov, Development of Detector Control System (DCS) for forward hadron
- 1110 calorimeters in the BM@N and the MPD experiments, J.Phys.Conf.Ser. 1690 (2020) 1, 012063,
- 1111 DOI: 10.1088/1742-6596/1690/1/012063
- 1112 [13] D. Baranov *et al.* GEM tracking system of the BM@N experiment, 2017 JINST 12 C06041.
- 1113 DOI 10.1088/1748-0221/12/06/C06041.
- 1114 [14] A. Galavanov *et al.* Status of the GEM/CSC tracking system of the BM@N experiment, 2020
- 1115 JINST 15 C09038. DOI 10.1088/1748-0221/15/09/C09038.
- 1116 [15] A. Galavanov *et al.* Performance of the BM@N GEM/CSC tracking system at the Nuclotron
- 1117 beam, 2019 EPJ Web Conf. 204 07009, <https://doi.org/10.1051/epjconf/201920407009> .
- 1118 [16] D. Bederede *et al.* Nucl. Instr. and Meth. A 367 (1995) 88.
- 1119 [17] I. Augustin *et al.* Nucl. Instr. and Meth. A 403 (1998) 472.
- 1120 [18] RedHat. Optimizing RHEL 9 for Real Time for low latency operation.
- 1121 (https://access.redhat.com/documentation/en-us/red_hat_enterprise_linux_for_real_time/9)
- 1122 [19] S. Weil *et al.* Ceph: A Scalable, High-Performance Distributed File System. OSDI 201906:
- 1123 7th USENIX Symposium on Operating Systems Design and Implementation.
- 1124 (<https://ceph.com/assets/pdfs/weil-ceph-osdi06.pdf>)
- 1125 [20] Tango is an Open Source solution for SCADA and DCS.
- 1126 (<https://www.tango-controls.org/>)
- 1127 [21] PostgreSQL is a powerful, open source object-relational database.
- 1128 (<https://www.postgresql.org/>)
- 1129 [22] Grafana is a multi-platform open source analytics and interactive visualization web applica-
- 1130 tion.
- 1131 (<https://grafana.com/>)